

Topological superconductivity from doping a triplet quantum spin liquid in a flat band system

Manuel Fernández López,¹ Ben J. Powell,² and Jaime Merino¹

¹*Departamento de Física Teórica de la Materia Condensada,
Condensed Matter Physics Center (IFIMAC) and Instituto Nicolás Cabrera,
Universidad Autónoma de Madrid, Madrid 28049, Spain*

²*School of Mathematics and Physics, The University of Queensland, QLD 4072, Australia*

(Dated: October 12, 2022)

We explore superconductivity in strongly interacting electrons on a decorated honeycomb lattice (DHL). An easy-plane ferromagnetic interaction arises from spin-orbit coupling in the Mott insulating phase, which favors a triplet resonance valence bond spin liquid state. Hole doping leads to partial occupation of a flat band and to triplet superconductivity. The order parameter is highly sensitive to the doping level and the interaction parameters, with $p + ip$, f and $p + f$ superconductivity found, as the flat band leads to instabilities in multiple channels. Typically, first order transitions separate different superconducting phases, but a second order transition separates two time reversal symmetry breaking $p + ip$ phases with different Chern numbers ($\nu = 0$ and 1). The Majorana edge modes in the topological ($\nu = 1$) superconductor are almost localized due to the strong electronic correlations in a system with a flat band at the Fermi level. This suggests that these modes could be useful for topological quantum computing. The ‘hybrid’ $p + f$ state does not require two phase transitions as temperature is lowered. This is because the symmetry of the model is lowered in the p -wave phase, allowing arbitrary admixtures of f -wave basis functions as overtones. We show that the multiple sites per unit cell of the DHL, and hence multiple bands near the Fermi energy, lead to very different nodal structures in real and reciprocal space. We emphasize that this should be a generic feature of multi-site/multi-band superconductors.

I. INTRODUCTION

Understanding the mechanism of superconductivity in strongly correlated materials remains a formidable challenge. For instance, high- T_c cuprates [1–3], organics [4] and twisted bilayer graphene [5, 6] (TBG), display similar phase diagrams [7]. In these materials superconductivity emerges near to a Mott insulating phase, indicating the important role played by strong correlations on Cooper pairing. A common ingredient in these systems is the presence of antiferromagnetic interactions, which lead to Mott insulators with antiferromagnetic order, as in the cuprates, or quantum spin liquids, as in the organic materials κ -(BEDT-TTF)₂Cu(CN)₃ or κ -(BEDT-TTF)₂Ag(CN)₃ [4, 8, 9]. Such AF interaction is crucial to singlet d -wave (or $d + id$) superconductivity which, according to Anderson’s theory of high- T_c superconductivity [10], can emerge when hole doping the resonance valence bond (RVB) Mott insulator on the square (triangular [11]) lattice [12]. The discovery of superconductivity in magic angle TBG [6] poses new questions about strongly correlated superconductivity in flat bands [13].

Definitive signatures of triplet pairing are rare outside the well understood triplet superfluidity [14, 15] in ³He. At present, there is no unambiguous evidence for, and increasing evidence against, triplet pairing in (former) candidate materials such as Sr₂RuO₄ [16–18], the quasi-one-dimensional (TMTSF)₂X Bechgaard salts [19] or A₂Cr₃As₃ [20, 21], (A=K, Rb, Cs). A reason for the scarcity of triplet superconductors is the antiferromagnetic (AFM) superexchange between spins which often dominates over ferromagnetic exchange processes, likely

to stabilize triplet superconductivity. However, the superconductivity observed [22] in the ferromagnetic Mott insulators, CrXTe₃ with $X = \text{Si, Ge}$ has been predicted to be of the triplet type [23]. Perhaps the most promising class of materials for observing triplet superconductors are the uranium based heavy fermion materials [24, 25], where superconductivity is often found near ferromagnetism.

Quantum spin liquids with ferromagnetic interactions cannot be described through standard singlet RVB theory. However, recent extensions to easy-plane ferromagnetic triangular lattices predict the existence of triplet resonance valence bond (tRVB) Mott insulators which can become unconventional $p + ip$ -wave superconductors under hole doping [23]. On the other hand, in multi-orbital systems such as the iron pnictides, Hund’s coupling can induce an intra-atomic triplet RVB state [26]. In these cases, triplet superconductivity may arise under hole doping. This is allowed by the presence of an even number of atoms per unit cell, leading to a spatially staggered gap pattern, as proposed by Anderson [27] in the context of heavy fermion superconductivity.

Triplet pairing induced by ferromagnetic interactions may arise in certain organic and organometallic materials with unit cells containing many atoms. (EDT-TTF-CONH₂)₆[Re₆Se₈(CN)₆] [28], Mo₃S₇(dmit)₃ [29], and Rb₃TT·2H₂O [30] crystals with layers of decorated honeycomb lattices (DHLs) can potentially host rich physics arising from the interplay of strong correlations, Dirac points, quadratic band touching points and flat bands [31–35]. This lattice also occurs in several metal organic frameworks and coordination polymers [35]. Indeed, un-

conventional *singlet* f -wave pairing has been found in an AFM t - J model on the DHL [36]. However, the spin molecular-orbital coupling (SMOC) present in these systems,[37–40] can lead to easy-plane ferromagnetic interactions favoring tRVB states. Hence, it is interesting to address the question of whether triplet superconductivity emerges in a strongly correlated easy-plane ferromagnetic model on a DHL. The possibility of finding non-trivial topological superconductivity as well as the role played by the flat bands deserve special attention.

In this paper we study a t - J model on a DHL with XXZ interactions, which arise due to spin-orbit coupling. Exact diagonalization of small clusters shows that a tRVB spin liquid, is a competitive ground state of the model at half-filling. Hole doping this spin liquid state leads to partial occupation of a flat band. Based on this we apply the tRVB approach to search for superconductivity in the hole doped system. We find multiple triplet superconducting phases, including include $p + ip$, $p + f$, f . Presumably, the wide variety of superconducting phases is a consequence of the flat band leading to instabilities in multiple Cooper channels.

Interestingly, we find both topologically trivial and topological $p+ip$ superconductivity with Chern numbers, $\nu = 0$ and 1 respectively. These phases are separated by a continuous phase transition, where nodes appear in the otherwise fully gapped $p + ip$ order parameter. In the topological superconductor phase the single Majorana edge mode expected for $\nu = 1$ is almost localized since it traverses a tiny gap bounded by nearly flat bands.

We show that the $p + f$ state does not require a two superconducting phase transitions as the temperature is lowered. Rather the once the symmetry of the system is lowered by going into the p -wave superconducting phase, the p and f solutions belong to the same irreducible representation of the group describing the symmetry of the model. Therefore, p and f are overtones and the system can and does take advantage of this to lower its energy.

The DHL lattice has six sites per unit cell. Therefore, diagonalizing the Hamiltonian requires a Bogoliubov transformation, a Fourier transformation and a transformation from the multi-site basis to a multiband basis. We show that the latter leads to remarkably different nodal structures in real and reciprocal space. We emphasize that this is a very general phenomenon in multiband superconductors.

We show that, at strong coupling (low doping), where the magnetic exchange is dominant, real space pairing dominates, leading to order parameters that are fully gapped or have only isolated nodal points in reciprocal space. In contrast, at weak coupling (high doping), where the superconductivity is dominated by the kinetic energy, the superconducting gap displays nodal points in reciprocal space.

The paper is organized as follows: in Sec II we introduce the anisotropic t - J model on a DHL with XXZ magnetic exchange interactions. In Sec. III we show, using exact diagonalization of small clusters, that a tRVB

spin liquid, is a competitive ground state of the model at half-filling. In Sec. IV we show that a wide variety triplet superconducting states emerge on hole-doping the tRVB, including a topological superconductor (TSC), and give a detailed characterization of these states. In Sec. V we characterize the TSC by calculating the topological invariants and Majorana edge modes. Finally, in Sec. VI we conclude our work by summarizing our main results and their relevance to actual materials realizing DHLs.

II. MODEL

Our starting point is a t - J model with easy-plane XXZ ferromagnetic exchange on the DHL:

$$\begin{aligned} \mathcal{H} = & -t \sum_{\alpha ij \sigma} P_G \left(c_{\alpha i \sigma}^\dagger c_{\alpha j, \sigma} + c_{\alpha j \sigma}^\dagger c_{\alpha i \sigma} \right) P_G \\ & - t' \sum_{\langle A, B \rangle i \sigma} P_G \left(c_{A i \sigma}^\dagger c_{B i \sigma} + c_{B i \sigma}^\dagger c_{A i \sigma} \right) P_G \\ & - J \sum_{\alpha ij} \left(S_{\alpha i}^x S_{\alpha j}^x + S_{\alpha i}^y S_{\alpha j}^y - S_{\alpha i}^z S_{\alpha j}^z + \frac{1}{4} n_{\alpha i} n_{\alpha j} \right) \\ & - J' \sum_{\langle A, B \rangle i} \left(S_{A i}^x S_{B i}^x + S_{A i}^y S_{B i}^y - S_{A i}^z S_{B i}^z + \frac{1}{4} n_{A i} n_{B i} \right) \\ & + \mu \sum_{\alpha i \sigma} c_{\alpha i \sigma}^\dagger c_{\alpha i \sigma}, \end{aligned} \quad (1)$$

where $P_G = \prod_i (1 - n_{i\uparrow} n_{i\downarrow})$ is the Gutzwiller projection operator which excludes doubly occupied sites completely, $c_{\alpha i \sigma}^{(\dagger)}$ is the usual annihilation (creation) operator, and $S_{\alpha i}^r$ is the r th component of the spin operator. The α -index runs over the two triangular clusters, while i, j run over the three sites within each triangular clusters, with site numbering as illustrated in Fig. 1, and σ denotes the spin of the electron. Angled brackets indicate that the sums are restricted to (triangles that contain) nearest-neighbor sites. We are interested in the properties of the model close to half-filling, so we write the electron density $n = 1 - \delta$, where δ is the density of holes doped into the half-filled DHL. We fix $t = 1$ as the energy scale. The XXZ exchange couplings, $J, J' > 0$, lead to easy-plane ferromagnetic (FM) interactions and AFM longitudinal interaction.

A possible microscopic origin of the XXZ exchange interactions of model (1) can be found by considering a single s-like orbital with on site (Hubbard) interactions and SMOC. On transforming to real space SMOC is equivalent to an anisotropic Kane-Mele spin-orbit coupling. If we consider nearest neighbor (nn) interactions with a z component of the spin-orbit coupling only we have

$$\mathcal{H} = i\lambda \sum_{\langle \alpha i \beta j \rangle} (c_{\alpha i \uparrow}^\dagger c_{\beta j \uparrow} - c_{\alpha i \downarrow}^\dagger c_{\beta j \downarrow}) + U \sum_{i \alpha} n_{i \alpha \uparrow} n_{i \alpha \downarrow}, \quad (2)$$

where $n_{i \alpha \sigma} = c_{i \alpha \sigma}^\dagger c_{i \alpha \sigma}$. In the large- U limit, the Hubbard

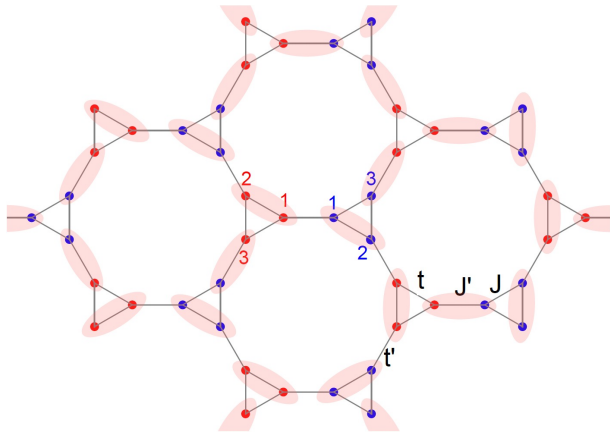


FIG. 1. The t - J model on the decorated honeycomb lattice. The unit cell consists of a A (red) and a B (blue) triangles with the sites numbered as shown. The parameters entering the model are illustrated. A particular triplet covering of the lattice entering the $|t\text{RVB}\rangle$ state of the model is shown.

model maps onto an effective XXZ spin hamiltonian [41]

$$\mathcal{H}_{\text{XXZ}} = -\frac{4\lambda^2}{U} \sum_{\langle\alpha i \beta j\rangle} \left(S_{\alpha i}^x S_{\beta j}^x + S_{\alpha i}^y S_{\beta j}^y - S_{\alpha i}^z S_{\beta j}^z \right). \quad (3)$$

At half-filling, the Hubbard model (2) with $U \gg |\lambda|$ becomes an XXZ model with $J = 4\lambda^2/U$, $J' = 4\lambda'^2/U$, i.e. Eq. (1), as is corroborated by our exact denatation-alization (ED) calculations of Appendix D. On including direct the hopping terms t and t' additional AFM exchange, Dzyaloshinskii-Moriya, and off diagonal exchange interactions will be introduced [37, 42, 43]. We neglect these interactions for simplicity. Thus Eq. (1) is a toy model for understanding the impact of SMOC on superconductivity. We further assume that $\lambda \propto t$ and $\lambda' \propto t'$ so that $J'/J = (t'/t)^2$ reducing the number of independent parameters in our Eq. (1). Other mechanisms for easy-plane ferromagnetic interaction have also been put forward recently, including interactions arising from the interplay of Hund's and Kondo interactions in heavy fermions.[44]

We emphasize that different materials are known to span a wide range of the parameter space for this model. For example, in $\text{Mo}_3\text{S}_7(\text{dmit})_3$ is in the trimerized limit: $t' < t$ and $J' < J$ [38, 45], whereas in $(\text{EDT-TTF-CONH}_2)_6[\text{Re}_6\text{Se}_8(\text{CN})_6]$ [28] and $\text{Rb}_3\text{TT}\cdot 2\text{H}_2\text{O}$ [30] are in the dimerized limit: $t' > t$ and $J' > J$. The physics of these two limits is known to differ markedly [32, 35]. Furthermore, at ambient pressure, $(\text{EDT-TTF-CONH}_2)_6[\text{Re}_6\text{Se}_8(\text{CN})_6]$ undergoes a metal-insulator transition as the temperature is lowered [28], whereas $\text{Mo}_3\text{S}_7(\text{dmit})_3$ [29] and $\text{Rb}_3\text{TT}\cdot 2\text{H}_2\text{O}$ [30] are insulating at all temperatures at ambient pressure.

III. TRIPLET RVB QUANTUM SPIN LIQUID

We analyze the ground state of model (1) by using tRVB theory[46], which has recently applied to iron pnictides[26] and transition metal chalcogenides[23]. It is analogous to Andersons RVB theory of high- T_c superconductivity to deal with strongly correlated models containing ferromagnetic exchange. Triplets rather than singlet bonds are the building blocks of the theory. The simplest form of the theory assumes that the ground state of the ferromagnetic undoped model is a quantum spin liquid in which spins are paired into triplets.

In general, such triplet RVB state can be expressed as:

$$|t\text{RVB}\rangle = \sum_P A_P |P_t\rangle, \quad (4)$$

where $|P_t\rangle = \prod_{ij \in P} |ij\rangle$ and the $S_z = 0$ spin triplet between sites i, j is

$$|ij\rangle \equiv \frac{|i, \uparrow\rangle |j, \downarrow\rangle + |i, \downarrow\rangle |j, \uparrow\rangle}{\sqrt{2}}, \quad (5)$$

where $|ij\rangle = -|ji\rangle$ due to the symmetry of triplets under inversion. Hence, the $|t\text{RVB}\rangle$ state is a quantum superposition of all possible coverings of the lattice into triplet valence bonds. The simplest version of the $|t\text{RVB}\rangle$ state involves triplets between nn spins only. One possible snapshot triplet configuration $|P_t\rangle$ entering $|t\text{RVB}\rangle$ is shown in Fig. 1.

A. Exact analysis of the triplet RVB in the DHL

We first concentrate on model (1) at half-filling, $\delta = 0$, which becomes a easy-plane XXZ ferromagnetic model. Triplet RVB states in such spin model are explored by performing exact diagonalization on six-site (two-triangle) clusters. The dependence of the exact level spectra of the cluster with J'/J is shown in Fig. 2(a). For any $J'/J \neq 0$ the four-fold ground state degeneracy found at $J' = 0$ is split so that the ground state becomes a non-degenerate $S = 1, S_z = 0$ triplet, as expected. The first excitation corresponds to a $S = 1, S_z = \pm 1$ doublet. The splitting between the $S = 1, S_z = 0$ and $S = 1, S_z = \pm 1$ states is increased by J'/J . The ground state energy at $J' = J$ is $\epsilon_0(\text{exact}) = -3.541287J$, and the corresponding wavefunction is given in the Appendix B.

We now consider a simple nn tRVB ansatz for the ground state wavefunction of the cluster, which consists on a linear combination of nn triplet valence bonds (VB) only:

$$\begin{aligned} |t\text{RVB}\rangle = & |A1B1\rangle |A2A3\rangle |B2B3\rangle + |A1A3\rangle |A2B2\rangle |B1B3\rangle \\ & + |A1A2\rangle |A3B3\rangle |B1B2\rangle - |A1B1\rangle |A2B2\rangle |A3B3\rangle, \end{aligned} \quad (6)$$

with the corresponding energy

$$\epsilon_0(\text{nn-tRVB}) = \frac{\langle \text{nn-tRVB} | \mathcal{H}_{\text{XXZ}} | \text{nn-tRVB} \rangle}{\langle \text{nn-tRVB} | \text{nn-tRVB} \rangle}. \quad (7)$$

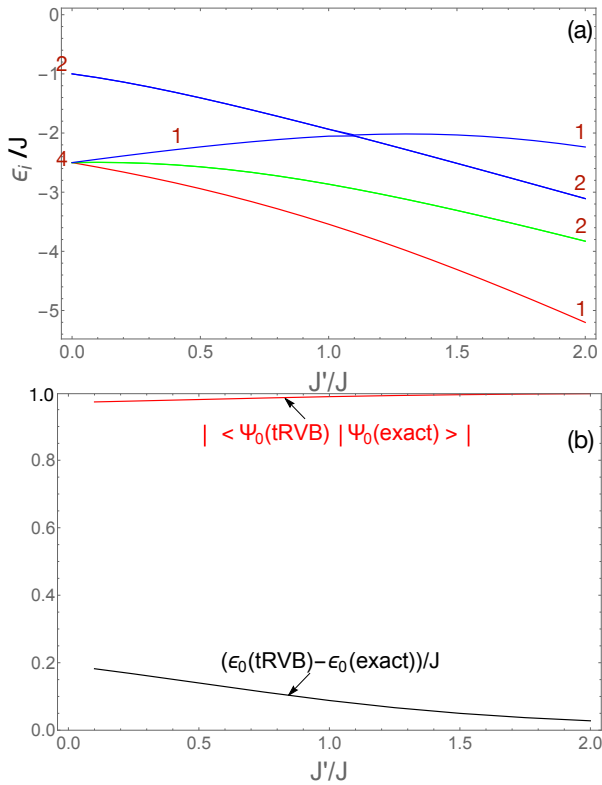


FIG. 2. Exact triplet RVB analysis of the half-filled easy-axis XXZ ferromagnetic model on a six site (two triangle) cluster. (a) The dependence of the low energy spectrum of the model (1) on J'/J . The numbers denote the exact energy level degeneracies. (b) The overlap between the exact ground state and the tRVB wavefunction for the six site cluster (given in Eq. (8)), $|\langle \Psi_0(\text{tRVB}) | \Psi_0(\text{exact}) \rangle|$, and the difference between the exact ground state energy, $\epsilon_0(\text{exact})$, and the triplet RVB energy, $\epsilon_0(\text{tRVB})$.

For $J' = J$ the overlap with the exact ground state is $\langle \Psi_0(\text{exact}) | \text{nn-tRVB} \rangle = 0.9747$, its energy is $\epsilon_0(\text{nn-tRVB}) = -3.397058J$ which is 4.07% higher than the exact ground state energy. In contrast, an RVB analysis of the Heisenberg antiferromagnetic model on the same cluster using nn singlet VBs would give a much more accurate description of the exact ground state: $\langle \Psi_0^{\text{HAFM}}(\text{exact}) | \text{nn-RVB} \rangle = 0.9988$ and $\epsilon_0^{\text{HAFM}}(\text{nn-RVB}) = -3.04412J$. The energy of this RVB state is only 0.16% higher than the exact ground state energy, $\epsilon_0^{\text{HAFM}}(\text{exact}) = -3.052775J$. Hence, it appears that the nn RVB gives a much better description of the ground state of the AFM Heisenberg model than the nn-tRVB of the easy-plane XXZ magnetic exchange we consider in this work.

We therefore consider a more general nn tRVB ansatz:

$$|\text{tRVB}\rangle = \alpha (|A1B1\rangle|A2A3\rangle|B2B3\rangle + |A1A3\rangle|A2B2\rangle|B1B3\rangle + |A1A2\rangle|A3B3\rangle|B1B2\rangle) - \beta |A1B1\rangle|A2B2\rangle|A3B3\rangle, \quad (8)$$

where α and β are determined variationally. For $J' = J$ we find an energy of $\epsilon_0(\text{tRVB}) = -3.453257J$ which is only 2.5% higher than the exact ground state energy. The overlap with the exact wavefunction is now $\langle \Psi_0(\text{exact}) | \text{tRVB} \rangle = 0.98849$, improving our previous result. For comparison a singlet-RVB

version of (8) for the Heisenberg antiferromagnet (HAF) recovers its exact ground state, i.e., $\langle \text{RVB} | \Psi_0^{\text{AFM}}(\text{exact}) \rangle = 1$, with an energy $\epsilon_0(\text{RVB}) = \epsilon_0^{\text{AFM}}(\text{exact}) = -5.302775J$.

We extend the variational |tRVB⟩ analysis to other $J' \neq J$. The dependence of the overlap and the energy difference on J'/J shown in Fig. 2(b) indicates that the |tRVB⟩ (Eq. (8)) becomes a closer description of the exact ground state of the cluster as J'/J increases since $\langle \text{tRVB} | \Psi_0(\text{exact}) \rangle \rightarrow 1$ and $\epsilon_0(\text{tRVB}) - \epsilon_0(\text{exact}) \rightarrow 0$. Furthermore, the large overlap found $\langle \text{tRVB} | \Psi_0(\text{exact}) \rangle \sim 1$ between the tRVB state and the exact ground state in the whole $J'/J > 0$ range explored indicates that the |tRVB⟩ is a good candidate for the ground state of the model.

The properties of quantum dimer models [47, 48] are independent of whether the dimers represent singlets or triplets. This suggests that dimerised states will be common to both singlet and triplet RVB theories. Therefore, it is interesting to note that two different valence bond solids are found in the antiferromagnetic Heisenberg model on the DHL: a valence bond solid with the full symmetry of the lattice for $J' \gtrsim J$ and a valence bond solid with broken C_3 symmetry for $J' \lesssim J$ [35, 49].

IV. TRIPLET RVB SUPERCONDUCTIVITY

Having established the tRVB state as a competitive ground state of the undoped model (1), we now consider the possibility of superconductivity mediated by the ferromagnetic part of the XXZ interaction. We first describe the pairing states allowed by the symmetries of the DHL. The most favorable superconducting states are then determined by a microscopic calculation. [23, 26]

A. Symmetry group analysis of superconducting states

A general phenomenological formulation of superconductivity can be achieved using Ginzburg-Landau theory in which the order parameter is obtained from general symmetry arguments. The full symmetry group of our model (1) is $C_{6v} \otimes \mathcal{K} \otimes U(1) \otimes SU(2)$ where \mathcal{K} is the time-reversal symmetry group.

On doping the triplets pairs in the tRVB wavefunction become mobile leading to triplet superconductivity. Note that this condensate contains only opposite spin pairing (OSP), in contrast to the equal spin pair (ESP) found in, say, the A-phase of ^3He [15]. Thus, one can fully describe the superconductivity by a scalar order parameter $\Delta(\mathbf{k})$ instead of requiring the usual vector order parameter for a triplet superconductor, $\mathbf{d}(\mathbf{k})$. However, these are trivially related via $\mathbf{d}(\mathbf{k}) = \Delta(\mathbf{k})\hat{\mathbf{z}}$, where $\hat{\mathbf{z}}$ is the unit vector in the longitudinal direction in spin-space. Thus, all states consider also break the $SU(2)$ symmetry associated with spin rotation. This is unsurprising as the XXZ interaction arises from spin-orbit coupling.

We conveniently [50] express the elements of the C_{6v} group in a 18-dimensional space generated by the pairing amplitudes, $\Delta_{\alpha i \sigma, \beta j \sigma'} = \langle c_{\alpha i \sigma} c_{\beta j \sigma'} \rangle$ consistent with the translational symmetry of the lattice. Defining the 18-component

short name	Γ	E	$2C_6$	$2C_3$	C_2	$3\sigma_v$	$3\sigma_d$	Singlet superconducting order	Triplet superconducting order
s	A_1	1	1	1	1	1	1	$[(1, 1, 1), (0, 0, 0), (1, 1, 1)],$ $[(0, 0, 0), (1, 1, 1), (0, 0, 0)]$	
i	A_2	1	1	1	1	-1	-1		$[(1, 1, 1), (0, 0, 0), (1, 1, 1)]$
f	B_1	1	-1	1	-1	1	-1	$[(-1, -1, -1), (0, 0, 0), (1, 1, 1)]$	$[(0, 0, 0), (-1, -1, -1), (0, 0, 0)]$
f'	B_2	1	-1	1	-1	-1	1		$[(1, 1, 1), (0, 0, 0), (-1, -1, -1)]$
p	E_1	2	1	-1	-2	0	0	$[(1, 0, -1), (0, 0, 0), (-1, 0, 1)],$ $[(1, -1, 0), (0, 0, 0), (-1, 1, 0)]$	$[(1, 0, -1), (0, 0, 0), (-1, 0, 1)],$ $[(1, -1, 0), (0, 0, 0), (-1, 1, 0)],$ $[(0, 0, 0), (2, -1, -1), (0, 0, 0)],$ $[(0, 0, 0), (0, 1, -1), (0, 0, 0)]$
d	E_2	2	-1	-1	2	0	0	$[(-1, 0, 1), (0, 0, 0), (-1, 0, 1)],$ $[(-1, 1, 0), (0, 0, 0), (-1, 1, 0)],$ $[(0, 0, 0), (-2, 1, 1), (0, 0, 0)],$ $[(0, 0, 0), (0, -1, 1), (0, 0, 0)]$	$[(1, 0, -1), (0, 0, 0), (1, 0, -1)],$ $[(1, -1, 0), (0, 0, 0), (1, -1, 0)]$

TABLE I. Character table of the C_{6v} with a list of the basis pairing functions allowed by symmetry in the singlet and triplet channels. The basis functions are expressed in terms of triplet/singlet pairing between nn sites of the lattice following the definitions of Fig. 3 and Eq. (12).

vector

$$\begin{aligned} \Delta_{\uparrow\downarrow} = & (\Delta_{A1\uparrow, A2\downarrow}, \Delta_{A2\uparrow, A1\downarrow}, \Delta_{A1\uparrow, A3\downarrow}, \Delta_{A3\uparrow, A1\downarrow}, \\ & \Delta_{A2\uparrow, A3\downarrow}, \Delta_{A3\uparrow, A2\downarrow}, \Delta_{A3\uparrow, B3\downarrow}, \Delta_{B3\uparrow, A3\downarrow}, \\ & \Delta_{A2\uparrow, B2\downarrow}, \Delta_{B2\uparrow, A2\downarrow}, \Delta_{A1\uparrow, B1\downarrow}, \Delta_{B1\uparrow, A1\downarrow}, \\ & \Delta_{B1\uparrow, B2\downarrow}, \Delta_{B2\uparrow, B1\downarrow}, \Delta_{B1\uparrow, B3\downarrow}, \Delta_{B3\uparrow, B1\downarrow}, \\ & \Delta_{B2\uparrow, B3\downarrow}, \Delta_{B3\uparrow, B2\downarrow}), \end{aligned} \quad (9)$$

the action of a group element in this representation, $R(a)$, on the pairing vector reads

$$\Delta'_{\uparrow\downarrow} = R(a)\Delta_{\uparrow\downarrow}. \quad (10)$$

Since spin is explicitly retained in the pairing amplitudes this nomenclature allows one to consider both singlet and OSP triplet states combinations simultaneously. From the $R(a)$ obtained for all the elements, a , of the C_{6v} character Table I we can obtain the projector operators on each of its irreducible representations

$$P^{(\mu)} = \frac{d_\mu}{g} \sum_a \chi^{(\mu)*}(a) R(a) \quad (11)$$

where $\chi^{(\mu)}(a)$ is the character of the a th element in the μ th irreducible representation, d_μ is the dimension of the irreducible representation μ , and g is the number of symmetry elements of the group.

The representation of the $g = 12$ elements of the C_{6v} symmetry group in the space spanned by the pairing amplitudes consists of twelve 18×18 matrices. The eigenvectors of the projector, $P^{(\mu)}$, with eigenvalue 1 describe basis functions of the six irreducible representations of the C_{6v} group. These basis functions are included in Table I. The pairing amplitudes between the sites given in Table I are expressed in terms of a three-component vector of three-component vectors,

$$\Delta = [\Delta_A, \Delta_X, \Delta_B], \quad (12a)$$

where,

$$\Delta_A = (\Delta_{A1, A2}, \Delta_{A3, A1}, \Delta_{A2, A3}), \quad (12b)$$

$$\Delta_X = (\Delta_{A3, B3}, \Delta_{A2, B2}, \Delta_{A1, B1}), \quad (12c)$$

$$\Delta_B = (\Delta_{B1, B2}, \Delta_{B3, B1}, \Delta_{B2, B3}), \quad (12d)$$

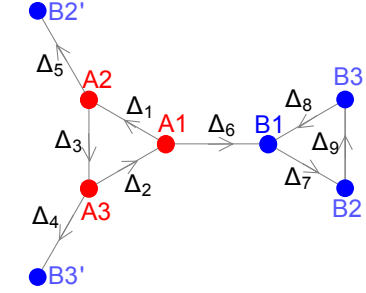


FIG. 3. Real space pairing amplitudes, encoded in the 9-dimensional vector, Δ , used in the mean-field analysis and linearized gap equations. The two triangular clusters in the unit cell are shown in red (A) and blue (B). For triplet superconductivity, the pairing amplitudes against the directions indicated by the arrows are minus the amplitudes along the arrow directions. In the singlet case arrows should be ignored since the pairing is non-directional.

where $\Delta_{\alpha i, \beta j} = (\Delta_{\alpha i \uparrow, \beta j \downarrow} + \Delta_{\alpha i \downarrow, \beta j \uparrow})/2$ for OSP triplet states and $\Delta_{\alpha i, \beta j} = (\Delta_{\alpha i \uparrow, \beta j \downarrow} - \Delta_{\alpha i \downarrow, \beta j \uparrow})/2$ for singlet pairing. The real space representation of Δ is sketched in Fig. 3. The arrows in Fig. 3 describe the antisymmetry of the triplet pairs, $\Delta_{\beta j, \alpha i} = -\Delta_{\alpha i, \beta j}$; for singlet pairing [51], $\Delta_{\beta j, \alpha i} = \Delta_{\alpha i, \beta j}$ and the order in which the bond is taken does not matter, so the arrows have no meaning and can be ignored.

B. Mean-field OSP triplet RVB theory

With the considerations above we explore the possibility of triplet RVB superconductivity in our model (1). We perform a mean-field BCS decoupling of the magnetic terms in the hamiltonian. It is convenient to write the theory in terms of triplet bond operators [26, 46],

$$h_{\alpha i, \beta j}^\dagger = \frac{1}{\sqrt{2}} (c_{\alpha i \uparrow}^\dagger c_{\beta j \downarrow}^\dagger + c_{\alpha i \downarrow}^\dagger c_{\beta j \uparrow}^\dagger). \quad (13)$$

Whence, the XXZ exchange in model (1) can be expressed as

$$\sum_{\langle\alpha i, \beta j\rangle} (S_{\alpha i}^x S_{\beta j}^x + S_{\alpha i}^y S_{\beta j}^y - S_{\alpha i}^z S_{\beta j}^z + \frac{n_{\alpha i} n_{\alpha j}}{4}) = \sum_{\langle\alpha i, \beta j\rangle} h_{\alpha i, \beta j}^\dagger h_{\alpha i, \beta j}, \quad (14)$$

We consider a BCS decoupling of the hamiltonian described through the pairing amplitudes:

$$\Delta_{\alpha i, \beta j} = \langle h_{\alpha i, \beta j} \rangle. \quad (15)$$

The mean-field hamiltonian with the renormalization effects due to the no double occupancy constraint, is then,

$$\mathcal{H}_{MF} = \mathcal{H}_t + \mathcal{H}_J \quad (16)$$

where:

$$\begin{aligned} \mathcal{H}_t &= -\tilde{t} \sum_{\mathbf{k}, \langle\alpha i, \alpha j\rangle, \sigma} (c_{\alpha i \sigma}^\dagger(\mathbf{k}) c_{\alpha j \sigma}(\mathbf{k}) + h.c.) - \tilde{t}' \sum_{\mathbf{k}, \langle A i, B i\rangle, \sigma} (e^{i\mathbf{k} \cdot \delta_{A i, B i}} c_{A i \sigma}^\dagger(\mathbf{k}) c_{B i \sigma}(\mathbf{k}) + h.c.), \\ \mathcal{H}_J &= -\frac{\tilde{J}}{\sqrt{2}} \sum_{\mathbf{k}, \langle\alpha i, \alpha j\rangle} (\Delta_{\alpha i, \alpha j} c_{\alpha i \uparrow}^\dagger(\mathbf{k}) c_{\alpha j \downarrow}^\dagger(-\mathbf{k}) - \Delta_{\alpha i, \alpha j} c_{\alpha j \uparrow}^\dagger(\mathbf{k}) c_{\alpha i \downarrow}^\dagger(-\mathbf{k})) + h.c. \\ &\quad - \frac{\tilde{J}'}{\sqrt{2}} \sum_{\mathbf{k}, \langle A i, B i\rangle} (\Delta_{A i, B i} e^{i\mathbf{k} \cdot \delta_{A i, B i}} c_{A i \uparrow}^\dagger(\mathbf{k}) c_{B i \downarrow}^\dagger(-\mathbf{k}) - \Delta_{A i, B i} e^{-i\mathbf{k} \cdot \delta_{A i, B i}} c_{B i \uparrow}^\dagger(\mathbf{k}) c_{A i \downarrow}^\dagger(-\mathbf{k})) + h.c. \\ &\quad + \tilde{J} \sum_{\langle\alpha i, \alpha j\rangle} |\Delta_{\alpha i, \alpha j}|^2 + \tilde{J}' \sum_{\langle A i, B i\rangle} |\Delta_{A i, B i}|^2 + \mu \sum_{\alpha \mathbf{k} \sigma} c_{\alpha \sigma}^\dagger(\mathbf{k}) c_{\alpha \sigma}(\mathbf{k}), \end{aligned} \quad (17)$$

where we have made the Gutzwiller approximation (GA), which yields renormalized parameters: $\tilde{t}/t = \tilde{t}'/t' = 2\delta/(1+\delta) \equiv g_t$ and $\tilde{J}/J = \tilde{J}'/J' = 4/(1+\delta)^2 \equiv g_J$. The numbering of sites in two neighboring A, B triangles together with the different pairing amplitudes entering the Gorkov decoupling are shown in Fig. 3.

After diagonalization, the hamiltonian reads

$$\begin{aligned} H_{MF} &= \sum_{m, \mathbf{k}, \sigma} \omega_m(\mathbf{k}) \left(\gamma_{m\sigma}^\dagger(\mathbf{k}) \gamma_{m\sigma}(\mathbf{k}) - \frac{1}{2} \right) \\ &\quad + \tilde{J} \sum_{\langle\alpha i, \alpha j\rangle} |\Delta_{\alpha i, \alpha j}|^2 + \tilde{J}' \sum_{\langle A i, B i\rangle} |\Delta_{A i, B i}|^2 \end{aligned} \quad (18)$$

where $\omega_m(\mathbf{k}) > 0$ with $m = 1, \dots, 6$ are the positive Bogoliubov quasiparticle dispersions.

The free energy of the system is

$$\begin{aligned} \Phi &= -\frac{1}{\beta} \sum_{m, \mathbf{k}, \sigma} \ln(1 + e^{-\beta \omega_m(\mathbf{k})}) - \sum_{m, \mathbf{k}} \omega_m(\mathbf{k}) + 6N_s \mu \\ &\quad + \tilde{J} \sum_{\langle\alpha i, \alpha j\rangle} (|\Delta_{\alpha i, \alpha j}|^2) + \tilde{J}' \sum_{\langle A i, B i\rangle} (|\Delta_{A i, B i}|^2) \end{aligned} \quad (19)$$

From the minimization of the free energy we arrive at a set of self-consistent equations (SCEs):

$$\begin{aligned} \Delta_{\alpha i, \alpha j} &= -\frac{1}{\tilde{J} N_s} \sum_{m, \mathbf{k}, \sigma} \left(f(\omega_m(\mathbf{k})) - \frac{1}{2} \right) \left(\frac{\partial \omega_m(\mathbf{k})}{\partial \Delta_{\alpha i, \alpha j}^*} \right), \\ \Delta_{A i, B i} &= -\frac{1}{\tilde{J}' N_s} \sum_{m, \mathbf{k}, \sigma} \left(f(\omega_m(\mathbf{k})) - \frac{1}{2} \right) \left(\frac{\partial \omega_m(\mathbf{k})}{\partial \Delta_{A i, B i}^*} \right), \\ \delta &= -\frac{1}{6N_s} \sum_{m, \mathbf{k}, \sigma} \left(f(\omega_m(\mathbf{k})) - \frac{1}{2} \right) \left(\frac{\partial \omega_m(\mathbf{k})}{\partial \mu} \right), \end{aligned} \quad (20)$$

which we solve numerically.

C. Phase diagrams and spinon dispersions

We now consider uniform metallic and superconducting solutions of the SCEs (20). As in singlet RVB theory, there are two temperature scales: T_{RVB} and T_{BEC} , which signify the onset of fermionic pairing and coherence respectively (the latter corresponds to Bose-Einstein condensation in the slave boson reformulation of theory [52]).

tRVB theory allows us to characterize the superconducting states emerging in the t - J model for different J'/J and δ . The phase diagrams of the $J' = J$ and $J' = 1.5J$ are shown in Fig. 4. The phase diagrams share similar qualitative features. At zero doping there is a ferromagnetic quantum spin liquid [37]. For $T < T_{\text{RVB}}, T_{\text{BEC}}$ there is pairing and coherence, so we have triplet superconducting phases. For $T_{\text{RVB}} < T < T_{\text{BEC}}$ there is coherence but no pairing, and we have a conventional Fermi liquid. For $T_{\text{RVB}}, T_{\text{BEC}} < T$ there is neither pairing nor coherence, so we have a strange metal. All of these phases are closely analogous to the phases in the same regimes of the singlet RVB theory [2].

However, for $T_{\text{BEC}} < T < T_{\text{RVB}}$, there is pairing but no coherence. In the singlet RVB theory this is interpreted as a spin gap or pseudogap [2]. In the tRVB theory we need to take care as we are dealing with triplet, rather than singlet, pairs. Furthermore, the strong SMOC assumed in the derivation of the XXZ model (Eq. (3)) implies that the ‘spins’ in our model are actually spin-orbit entangled pseudospins. Therefore, we expect a gap for longitudinal magnetic fields, but no gap for transverse magnetic fields in the tRVB pseudogap phase. This contrasts with the singlet-RVB state where the (pseudo)gap is apparent for any magnetic field direction. For the tRVB state for sufficiently large longitudinal fields (relative to the strength of the spin-orbit coupling) we expect, on general energetic grounds, a transition where the triplet order parameter rotates to be perpendicular to the field [53], this is analogous Fréedericksz transition in liquid crystals and ^3He in slab geometries [54].

In both cases at the larger dopings at which weak coupling

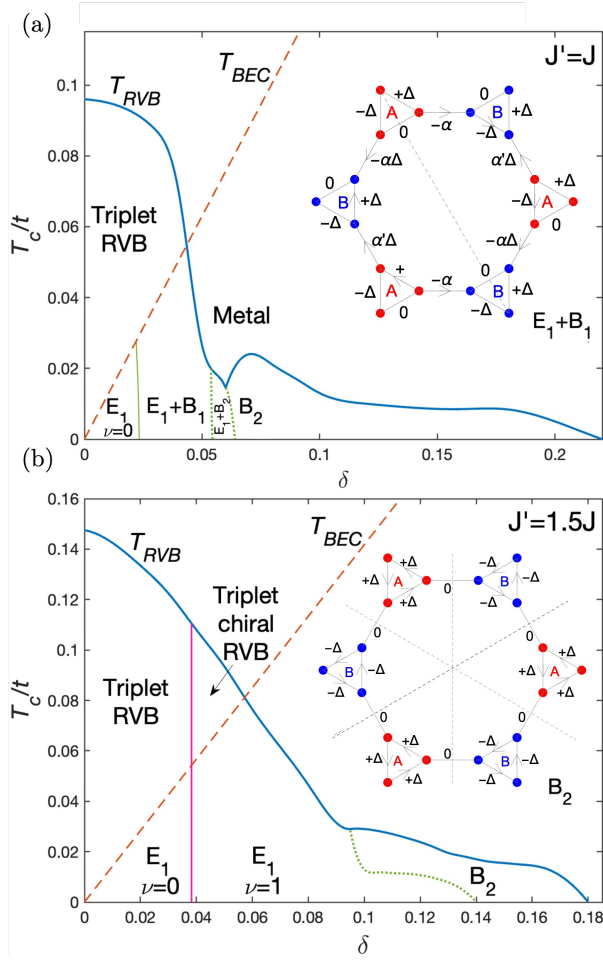


FIG. 4. T vs δ phase diagrams of the t - J model (1) from triplet-RVB theory for (a) $J'/J = 1$ and (b) $J'/J = 1.5$. Superconductivity occurs when $T < T_{BEC}$ (red dashed line) and $T < T_{RVB}$ (blue line). While the transition at T_{RVB} (blue solid line) is second order, the transitions between different superconducting orders can be first (green dotted lines) or second (green solid lines) order. A second order topological transition (pink solid line) separates E_1 ($\nu = 0$) and E_1 ($\nu = 1$) in (b). The insets in (a) and (b) illustrate the pairing patterns of the $p + f$ ($E_1 + B_1$) and f (B_2) solutions including their nodal lines in real space (black dashed lines). We have used $J = 0.1t$ and $J'/J = t'^2/t^2$.

theory is relevant the most stable superconducting solution has f -wave (B_2) symmetry,

$$\Delta(B_2) = [(1, 1, 1), (0, 0, 0), (-1, -1, -1)], \quad (21)$$

which is sketched in the inset of Fig. 4(b). As expected, given the scalar order parameter, this f -wave triplet superconducting solution displays three nodal lines in real space.

In the strong coupling regime, $\delta \rightarrow 0$, a $p + ip$ (E_1) superconducting phase is found to be the ground state for both exchange $J'/J = 1$ and $J'/J = 1.5$. This state displays a

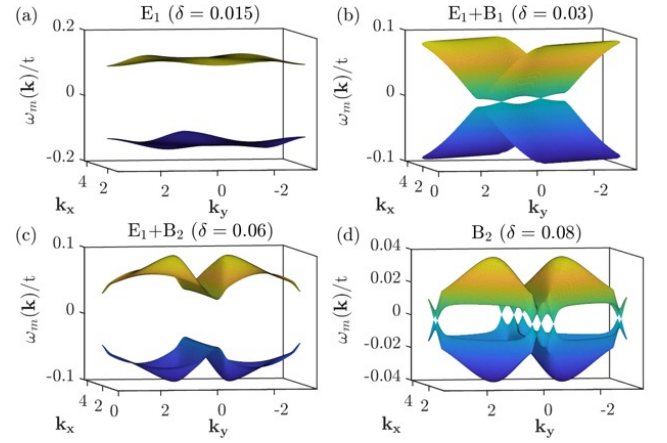


FIG. 5. Mean-field BdG bands at a fixed temperature $T = 0.01t$ for the different pairing symmetries at $J'/J = 1$. Only the occupied, $-\omega_1(\mathbf{k})$, and unoccupied, $\omega_1(\mathbf{k})$, bands closest to the Fermi level are shown for simplicity.

complex order parameter given by:

$$\begin{aligned} \Delta(E_1) = & [(1, 0, -1), (0, 0, 0), (-1, 0, 1)] \\ & + e^{i\alpha_1} [(1, -1, 0), (0, 0, 0), (-1, 1, 0)] \\ & - \Delta' (e^{i\alpha_2} [(0, 0, 0), (2, -1, -1), (0, 0, 0)] \\ & + \sqrt{3} e^{i\alpha_1} [(0, 0, 0), (0, 1, -1), (0, 0, 0)]), \quad (22) \end{aligned}$$

with lightly δ -dependent phases around $\alpha_1 = \pi/3$ and $\alpha_2 = \pi/6$ (up to numerical accuracy) and the amplitude Δ' strongly dependent on the doping. Clearly, this state breaks time reversal symmetry.

However, important differences between the two phase diagrams appear in the intermediate doping range. For $J' = J$ the E_1 and B_2 pairing states are separated by two superconducting states obtained from the mixing of two different irreducible representations of Table I. At $\delta > 0.023$, a second order transition to a $p + f$ ($E_1 + B_1$) symmetry superconducting state occurs, where

$$\Delta(E_1 + B_1) = [(1, 0, -1), (-\alpha, \alpha', -\alpha), (-1, 0, 1)], \quad (23)$$

has the lowest energy. The intertriangle amplitudes ratio α'/α has a doping dependence which is analyzed in Appendix C (see especially Fig. 15). By raising the doping above $\delta \sim 0.053$ a first order transition to a $p + f'$ ($E_1 + B_2$) pairing state occurs, which order parameter reads

$$\Delta(E_1 + B_2) = [(1, 1, \eta), (-\xi, \xi, 0), (-1, -1, \eta)], \quad (24)$$

with $0 < \eta, \xi < 1$. Then at $\delta = 0.064$ the system transits to the pure f -wave (B_2) described above. These pairing states come from linear combinations of p (E_1) and f (either B_1 or B_2) superconducting solutions (see Table. I). These ‘hybrid’ superconducting states are forbidden in the linearized gap equations (see discussion of T_c s in the following subsection), as every solution must transform according to a single representation of C_{6v} [55]. However, when the superconducting state lowers the symmetry of the system to \mathcal{G} , a subgroup of C_{6v} , then any harmonic transforming according to the same irreducible representation of \mathcal{G} as the superconducting order parameter can mix without breaking additional symmetries

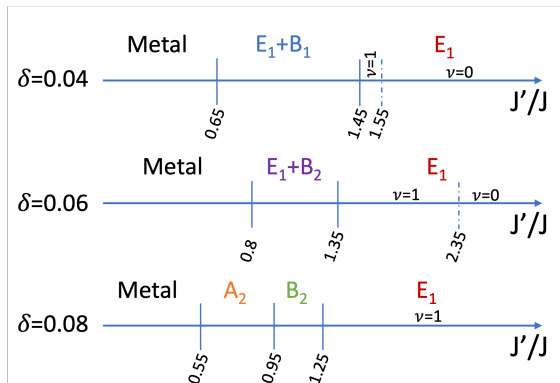


FIG. 6. Dependence of superconducting states on dimerization/trimerization, J'/J . The phase diagrams of model (1) at three different dopings: $\delta = 0.04, 0.06, 0.08$ are shown at fixed $T = 0.01$. We have used $J = 0.1t$ and $J'/J = t'^2/t^2$.

and hence causing a phase transition (immediately) below T_c . A full mathematical discussion of this is given in Appendix C based on the the general framework [55]. For p -wave (E_1) solutions on the DHL the only other representations of C_{6v} that can mix are f -wave (B_1 and B_2). Thus, in $p + f^{(\prime)}$ states are common on the DHL as they often have lower energy than pure p -wave states.

For $J' = 1.5J$ the complex $p + ip$ solution (22) survives for much higher dopings relegating the B_2 state to a small doping region. The E_1 superconducting parameter increases rapidly as doping decreases ($\|\Delta(E_1)\| \gg 1$ for $\delta \rightarrow 0$). Furthermore, we find a second order transition at $\delta_c = 0.039$ above which the $p + ip$ superconducting state becomes topologically non-trivial with a Chern number $\nu = 1$. The $p + ip$ (E_1) topological superconductor, will be discussed in detail in Sec. V.

The superconducting order parameter in reciprocal space can be quite different to its real space counterpart as expected in a multiband system.[50] In Fig. 5 we show the doping dependence of the lowest energy BdG excitations for $J' = J$. In marked contrast to one band systems, the nodal structure of the dispersions of the present multiband system (with many atoms per unit cell), is very different to the one in real space. For instance, the f -wave (B_2) solution of Fig. 5(d) displays only isolated nodal points in contrast to the three nodal lines occurring in real space. Similarly, the $p + f$ (E_1+B_1) state shown in 5(b) is characterized by two nodal points along $k_y = k_x$ in the BdG bands although the superconducting state has a single nodal line in real space (see inset of Fig. 4(a)). The $p + f$ (E_1+B_2) state is gapped over the entire Brillouin zone in contrast to the three nodal lines occurring in real space. Only in the $p + ip$ (E_1) superconducting phases the order parameter is found to be fully gapped consistently in real and reciprocal space as illustrated in Fig. 5(a) for $\delta = 0.015$. At the critical lines of the Fig. 4 phase diagrams separating E_1 solutions with different topological properties nodal points occur.

Thus an overall trend emerges: at strong coupling, $\delta \rightarrow 0$, when the system is dominated by magnetic exchange the SC is characterized by either having isolated nodal points or being fully gapped. In contrast, the weak coupling solutions at large δ are dominated by the kinetic energy and the gap has nodal points in reciprocal space. Hence, gapless superconductivity is more common in the weak coupling regime than at strong

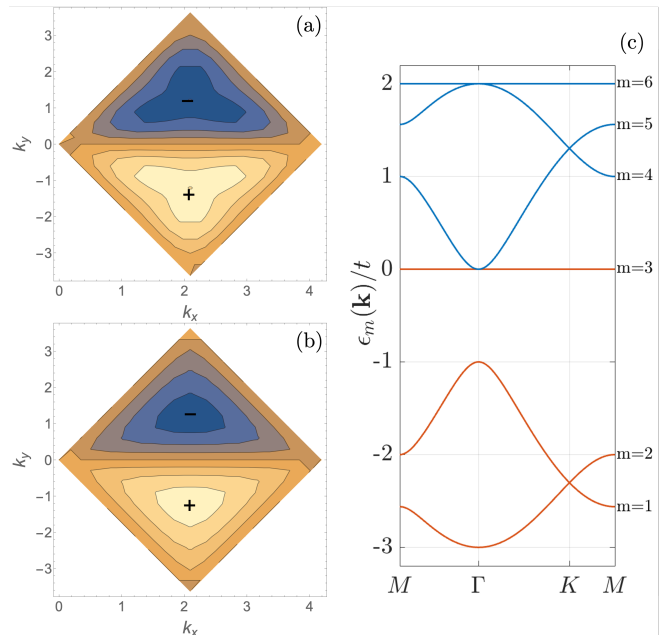


FIG. 7. Triplet gap function projected onto the occupied bands closest to Fermi energy. The intraband gaps, $\Delta_{22}(\mathbf{k})$ (a) and $\Delta_{33}(\mathbf{k})$ (b) corresponding to the f -wave (B_2) solution for $\delta = 0.09$ and $J' = J$ are shown. Note the different scale of the pairing amplitude in the two figures: (a) $-0.068-0.068$; (b) $-0.64-0.64$. (c) Bare bands (eigenstates of \mathcal{H}_t , Eq. (17) for $\tilde{t} = t = \tilde{t}' = t''$).

coupling.

Hybrid and topological superconductivity are not peculiar to the specific J'/J explored in Fig. 4. The phase diagrams of Fig. 6 show that the hybrid E_1+B_1 and E_1+B_2 states occur at low $\delta \sim 0.04-0.06$ in an extend range of J'/J , consistent with the analysis of Appendix C. At larger dopings, say $\delta = 0.08$, pure A_2 , B_2 and E_1 are favored, respectively, as J'/J increases consistent with the weak coupling analysis of Appendix A. On the other hand, topological $p + ip$ (E_1) superconductivity (with $\nu = 1$) is favored in the dimerized regime, $J'/J > 1$, and increasing δ , Fig. 6. As doping increases the topological transition to the trivial E_1 superconducting state ($\nu = 0$) occurs deeper into the dimerized limit. Hence, hybrid and topological superconductivity are robust solutions of the SCE of model (1).

D. Critical temperatures and superconducting pairing states

Additional understanding can be gained from a weak coupling microscopic analysis to obtain the T_c s of the different possible pairing solutions. The set of SCE (20) can be linearized by expanding the quasiparticle energies around T_c . This yields

$$\omega_m(\mathbf{k}) = \epsilon_m(\mathbf{k}) + \sum_n \frac{|\Delta_{mn}(\mathbf{k})|^2}{\epsilon_m(\mathbf{k}) + \epsilon_n(\mathbf{k})}, \quad (25)$$

where the $\epsilon_m(\mathbf{k})$ are the eigenvalues of the kinetic energy part of the mean-field part of the hamiltonian, \mathcal{H}_t , Eq. (17), with

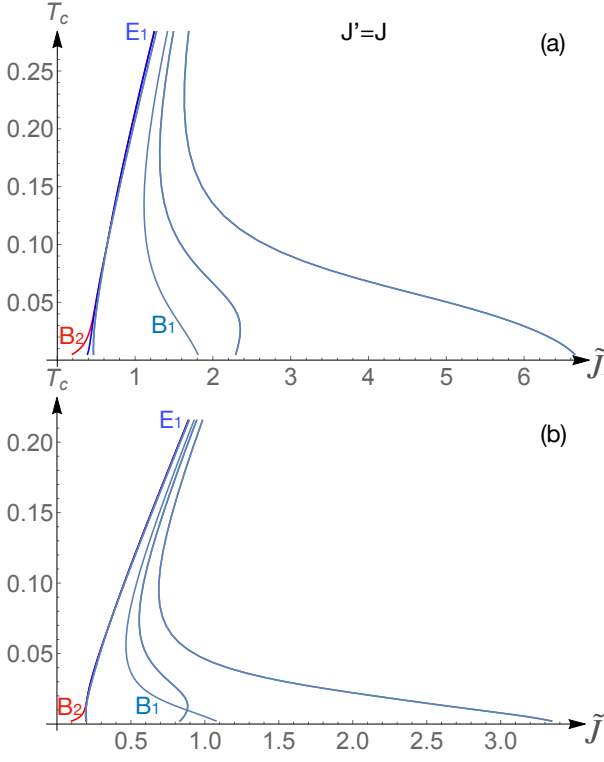


FIG. 8. Dependence of the superconducting critical temperatures on the strength of the magnetic coupling, \tilde{J} obtained from the linearized gap equations at $J' = J$ for doping (a) $\delta = 0.1$ and (b) $\delta = 0.04$. The most favorable solution at a given \tilde{J} occurs for the channel with the highest T_c . While the dominant superconducting solution at small coupling, $\tilde{J} \rightarrow 0$, is f -wave (B_2 ; red solid line), at large \tilde{J} , the doubly-degenerate p wave (E_1 ; magenta solid line) solution is found. $t = 1$ in these plots.

m running from the lowest to highest energy band (shown in Fig. 7(c)). The gap functions projected onto the different bands, $\Delta_{mn}(\mathbf{k})$, read:

$$\Delta_{mn}(\mathbf{k}) = \sum_p \tilde{J}_p \Omega_{mn}^p(\mathbf{k}) \Delta_p, \quad (26)$$

where m, n denote the different bands and $p = 1, \dots, 9$ with Δ_p , the real space Cooper pairing amplitudes of Eq. (12), shown in Fig. 3, and $\tilde{J}_p = \tilde{J}$ for $p = 1, 2, 3$ and $p = 7, 8, 9$ while $\tilde{J}_p = \tilde{J}'$ for $p = 4, 5, 6$, and the $\Omega_{mn}^p(\mathbf{k})$ are products of Bloch wavefunction coefficients defined in Eq. (A1). We can understand the differences between real and reciprocal space pairing by comparing the intra- and intra-band order parameters. The intraband gap functions, $\Delta_{mm}(\mathbf{k})$, for f -wave (B_2) solutions for $J' = J$ and $\delta = 0.09$ with $m = 2, 3$, shown in Fig. 7, provide a typical example. The solution in \mathbf{k} -space projected onto the flat band at the Fermi energy, $m = 3$, shows a p_y -wave structure (i.e., it is odd under $k_y \rightarrow -k_y$, but even under $k_y \rightarrow -k_x$) similar to the lowest energy BdG dispersion, Fig. 5(d). However, we also find large that the interband contributions, $|\Delta_{m3}(\mathbf{k})| \lesssim 0.22$ for $m \neq 3$, can be quite large compared to the intraband contribution $|\Delta_{33}(\mathbf{k})| \sim 0.64$. This is important for understand why the real space and reciprocal space

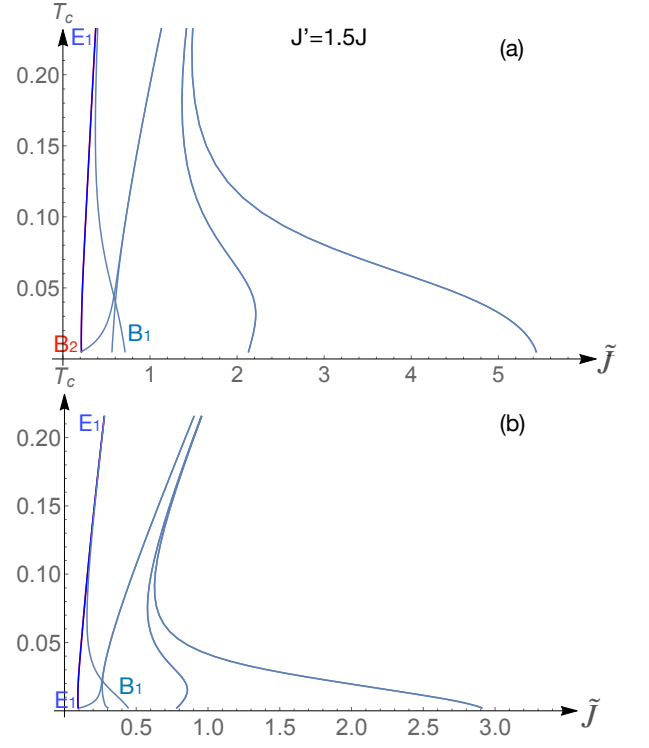


FIG. 9. Dependence of the superconducting critical temperatures on \tilde{J} obtained from the linearized gap equations at $J' = 1.5J$ for doping (a) $\delta = 0.1$ and (b) $\delta = 0.04$. While the dominant superconducting solution at weak coupling, $\tilde{J} \rightarrow 0$, the p -wave (E_1) and f -wave (B_2) solutions are degenerate within the accuracy of our calculations, for strong coupling the doubly-degenerate p -wave (E_1 ; magenta solid line) state has the highest T_c . $t = 1$ in these plots.

pictures are so different. Even more remarkably, for $p + f$ ($E_1 + B_1$) superconductivity, $\Delta_{33}(\mathbf{k}) = 0$, which means that, the interband contributions $|\Delta_{m3}(\mathbf{k})|$ are solely responsible the gap in the BdG spectrum, Fig. 5(b).

The set of linearized gap equations at T_c obtained by introducing the approximate BdG dispersions, $\omega_m(\mathbf{k})$ in Eq. (20), read

$$\Gamma \tilde{\Delta} = \frac{1}{\tilde{J}} \tilde{\Delta}, \quad (27)$$

where $\tilde{\Delta} = (\tilde{J}\Delta_A, \tilde{J}'\Delta_X, \tilde{J}\Delta_B)$. Solving for the eigenvalues of (27), $1/\tilde{J}^\lambda$, we can conveniently obtain the dependence of T_c on \tilde{J} in the different pairing channels: λ , described by the eigenvectors $\tilde{\Delta}_\lambda$ (see Appendix A for details). These eigenvectors can be classified according to the character table 1 as it should since the matrix Γ respects the C_{6v} point group symmetry of the lattice.

The elements of the 9×9 matrix Γ are

$$\Gamma_{pq} = \frac{1}{2N_s} \frac{\tilde{J}_p}{\tilde{J}} \sum_{m,n,\mathbf{k}} \tanh\left(\frac{\epsilon_m(\mathbf{k})}{2k_B T}\right) \frac{1}{\epsilon_m(\mathbf{k}) + \epsilon_n(\mathbf{k})} \times (\Omega_{mn}^{*p}(\mathbf{k})\Omega_{mn}^q(\mathbf{k}) + \Omega_{mn}^p(\mathbf{k})\Omega_{mn}^{*q}(\mathbf{k})). \quad (28)$$

We can gain insight into the phase diagrams of Fig. 4 obtained from the full SCE by analyzing the dependence of T_c on the strength of the coupling, \tilde{J} , as obtained from the linearized gap equation (27). The T_c s obtained from (27) for

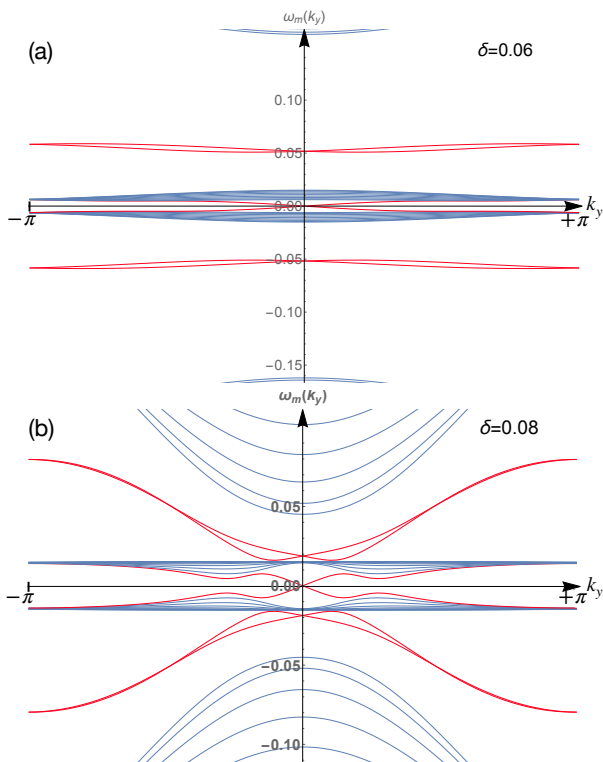


FIG. 10. Topological edge states in the TSC (E_1) phase. The BdG band structure of a superconducting ribbon with zig-zag edges along the y -direction is shown for $J' = 1.5J$ and $\delta = 0.06$ (top) and $\delta = 0.08$ (bottom). The gapped BdG bands (blue) are traversed by surface edge states (red) crossing at $k_y = 0$. Edge states are identified by direct comparison with the spectrum of the extended system. Note that as $t = 1$ in these plots, the Majorana modes are extremely localized (i.e., the Majorana bands are extremely flat).

$J' = J$ and $J' = 1.5J$ are shown in Figs. 8 and 9 respectively. From these plots one can obtain useful information about the dominant pairing channel which is given by the one with the largest T_c for a given \tilde{J} .

In the full phase diagrams of Fig. 4 as $\delta \rightarrow 0$ the effective coupling increases, $\tilde{J}/t \propto g_J/g_t \propto 1/\delta$ due to the effect of the GA projection. We consistently find that the f -wave (B_2) solution arises for large doping $\delta \sim 0.1 - 0.2$ in the solution of the SCEs indeed has the highest T_c in the linearized equations as $\tilde{J} \rightarrow 0$, Figs. 8(a) and 9(a). As \tilde{J} increases the E_1 has the highest T_c . However, the T_c 's of other solutions become very similar to the T_c of the E_1 solution. This means that several superconducting solutions are numerically indistinguishable. The E_1 , A_2 , and B_2 solutions have nearly identical T_c 's and the T_c of the B_1 solution becomes close to these as \tilde{J} increases. This is consistent with the full non-linear SCE which while for $J' = 1.5J$ give a pure E_1 solution, for $J' = J$ a E_1+B_1 combination eventually wins. The SCE also show that for $J' = 1.5J$ a complex combination of two E_1 is energetically favorable.

More details on the analysis of the T_c 's are provided in Appendix A.

The ED pairing correlations at $\delta = 0$ (see Appendix D) show that while the E_1 and B_1 solutions are dominant for

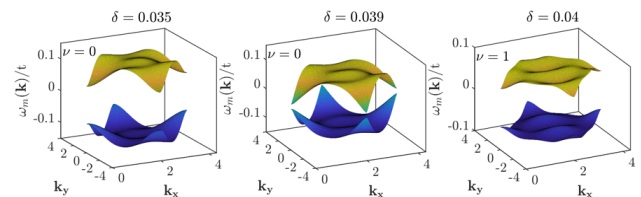


FIG. 11. Dependence of the BdG bands, $\pm\omega_1(\mathbf{k})$ on doping, δ , across the low doping topological transition for $J'/J = 1.5$. At $T = 0.01$ as δ increases from $\delta = 0$ a topological gap with $\nu = 1$ opens around $\delta_c \sim 0.385$ signalling the TSC(E_1) phase of Fig. 4.

$J'/J > 1/\sqrt{2}$, the A_2 and B_2 are favorable for $J'/J < 1/\sqrt{2}$. These limits are in good agreement with the present weak coupling analysis, considering the small six-site cluster analysed with ED.

V. TOPOLOGICAL SUPERCONDUCTIVITY

Unambiguous signatures of non-trivial topology are found in both the presence of topological edge states and a non-zero topological bulk invariant, as guaranteed by the bulk-boundary correspondence. In the case of time reversal symmetry breaking superconductors the topological invariant is the Chern number ν which we evaluated as described in Appendix E. We find that the $p + ip$ (E_1) TSC phase has a Chern number, $\nu = 1$, while the other phases discussed are non-topological, $\nu = 0$.

From the Chern number calculation we conclude that the $p + ip$ (E_1) TSC has a single Majorana edge mode circulating around the edge of the sample. We obtain the edge states of a ribbon in the zig-zag geometry cut along the y -direction assuming the lattice orientation shown in Fig. 1. The ribbon is assumed to be in a superconducting state with pairing amplitudes given by the bulk solution, i.e., we do not perform a fully self-consistent calculation of the ribbon. We plot the projected BdG bands along the k_y edge of a ribbon in the $p + ip$ (E_1) TSC state in Fig. 10. As well as the bulk bands, two edge states with opposite slopes (velocities) cross at $k_y = 0$ inside the gap around zero energy. These correspond to the chiral edge state circulating in opposite directions on the two edges of the ribbon as expected for $\nu = 1$. In contrast, no topological edge states are found in ribbons in the f -wave (B_2) and $p + f$ (E_1+B_1) superconducting phases as expected for $\nu = 0$. Interestingly, the Majorana edge modes associated with the $p + ip$ (E_1) TSC are almost localized since it emerges within a small gap in nearly flat bands.

A topological transition from the trivial $p + ip$ (E_1) superconductor to the topological $p + ip$ (E_1) superconductor occurs at $\delta_c \sim 0.039$ in the phase diagram 4 for $J' = 1.5J$. The smooth closing and reopening of the superconducting gap (see Fig. 11) is accompanied by the Chern number jump, $\Delta\nu = 1$, which indicates a second order topological transition at δ_c . At a larger δ ($\delta \approx 0.14$ at $T = 0.01t$), a first order transition from the $p + ip$ (E_1) TSC to the non-topological f -wave (B_2) phase occurs. This contrasts with the doped Kitaev model[56] in which only first order transitions between superconducting states occur. At temperatures above the condensation temperature, $T > T_{\text{BEC}}$, the second order transition at δ_c be-

comes a transition from a tRVB to a *chiral* tRVB quantum spin liquid (see Fig. 4).

VI. CONCLUSIONS

In this work we have found unconventional triplet superconductivity in an easy-axis XXZ ferromagnetic t - J model on the DHL. The underlying mechanism is attributed to the preexistence of a tRVB spin liquid in the Mott phase which is suggested by numerical exact diagonalization calculations. The symmetry of the superconducting order parameter depends sensitively on both J'/J and doping. This is a direct consequence of the flat band, which favors many superconducting channels.

At small δ ferromagnetic interactions dominate leading to exotic phases including topological superconductivity. However, at large δ superconductivity is mainly weak coupling, and strongly influenced by band structure effects. A similar situation including topological superconductivity was predicted for hole doped Kitaev spin liquids with ferromagnetic exchange interactions.[56]

Generically, lines of first order transitions separate different superconducting phases. The important exception to this is the transition from topologically trivial $p + ip$ (E_1) superconductivity to topological $p + ip$ (E_1) superconductivity with Chern number, $\nu = 1$. This transition is continuous, which is possible as both states transform according to the same irreducible representation of C_{6v} . This occurs in a two-dimensional representation is, perhaps, unsurprising in retrospect, as two-dimensional representations lead quite naturally to broken time reversal symmetry [57].

Topological superconductivity occurs in a broad doping range of the phase diagram being favored at large J'/J . Critical temperatures of $T_c \sim 0.8J$ are reached at optimal hole doping, $\delta \sim 0.06$ for $J' = 1.5J$. The corresponding Majorana edge modes obtained at the lowest dopings are almost localized in two flat bands close to the Fermi level. This suggests that topological superconductivity in flat band materials could be useful for decoherence free topological quantum computing schemes based on localized Majorana modes.

We have shown that the nodal structures of the superconducting gap appear very different in real space and reciprocal space. This results from the need to transform from a real-space multi-site basis to a reciprocal space multi-band basis. There is nothing special about the DHL lattice in this regard. Therefore, we expect this to be observed in any superconductor where multiple (atomic [50] or molecular) orbitals at distinct sites contribute significant density of states near the Fermi energy.

It is also interesting that we observed $p+f$ superconductivity with only a single superconducting transition even though p -wave and f -wave superconductors belong to different representations of C_{6v} – the point group describing the DHL, E_1 and B_1 or B_2 respectively. This occurs because the dominant p wave superconducting state lowers the symmetry of the system, such that the p -wave and f -wave belong to the same irreducible representation, i.e., they become overtones, and arbitrary admixtures are allowed without breaking additional symmetries. That this is possible has long been understood [15, 55], however there are still relatively few detailed calculations where this is observed.

A crucial ingredient of our model is the easy-plane ferro-

magnetic interaction which can arise in spin orbit Mott insulators. Although candidate materials such as $\text{Mo}_3\text{S}_7(\text{dmit})_3$, $(\text{EDT-TTF-CONH}_2)_6[\text{Re}_6\text{Se}_8(\text{CN})_6]$, and $\text{Rb}_3\text{TT}\cdot 2\text{H}_2\text{O}$ host strong correlations on a DHL antiferromagnetic interactions are dominant. Increasing SMOC in these candidate materials, for example by synthesizing the Se analogue of $\text{Mo}_3\text{S}_7(\text{dmit})_3$ or finding other spin orbit Mott insulators on DHLs are routes for realizing triplet superconductivity under hole doping. Hole doping has been achieved in certain organics[58] but only at a specific doping fixed by the chemistry of the constituents. Clearly, experimental progress in hole doping techniques are required to enlarge hole doping ranges in organic and organometallic materials and test our prediction of triplet topological superconductivity in the DHL.

ACKNOWLEDGMENTS

We acknowledge financial support from (RTI2018-098452-B-I00) MINECO/FEDER, Unión Europea and the Australian Research Council (DP180101483).

Appendix A: Superconducting critical temperatures and pairing symmetries

We now analyze the pairing symmetries and T_c s based on the weak coupling analysis of Section IV D of the main text. The matrix elements, $\Omega_{mn}^p(\mathbf{k})$ in Eq. (28) read:

$$\begin{aligned}\Omega_{mn}^1(\mathbf{k}) &= C_{A1}^*(\epsilon_m)C_{A2}(\epsilon_n) + C_{A2}^*(\epsilon_m)C_{A1}(\epsilon_n) \\ \Omega_{mn}^2(\mathbf{k}) &= C_{A1}^*(\epsilon_m)C_{A3}(\epsilon_n) + C_{A3}^*(\epsilon_m)C_{A1}(\epsilon_n) \\ \Omega_{mn}^3(\mathbf{k}) &= C_{A2}^*(\epsilon_m)C_{A3}(\epsilon_n) + C_{A3}^*(\epsilon_m)C_{A2}(\epsilon_n) \\ \Omega_{mn}^4(\mathbf{k}) &= C_{A1}^*(\epsilon_m)C_{B1}(\epsilon_n)e^{i\mathbf{k}\delta_1} + C_{B1}^*(\epsilon_m)C_{A1}(\epsilon_n)e^{-i\mathbf{k}\delta_1} \\ \Omega_{mn}^5(\mathbf{k}) &= C_{A2}^*(\epsilon_m)C_{B2}(\epsilon_n)e^{i\mathbf{k}\delta_2} + C_{B2}^*(\epsilon_m)C_{A2}(\epsilon_n)e^{-i\mathbf{k}\delta_2} \\ \Omega_{mn}^6(\mathbf{k}) &= C_{A3}^*(\epsilon_m)C_{B3}(\epsilon_n)e^{i\mathbf{k}\delta_3} + C_{B3}^*(\epsilon_m)C_{A3}(\epsilon_n)e^{-i\mathbf{k}\delta_3} \\ \Omega_{mn}^7(\mathbf{k}) &= C_{B1}^*(\epsilon_m)C_{B2}(\epsilon_n) + C_{B2}^*(\epsilon_m)C_{B1}(\epsilon_n) \\ \Omega_{mn}^8(\mathbf{k}) &= C_{B1}^*(\epsilon_m)C_{B3}(\epsilon_n) + C_{B3}^*(\epsilon_m)C_{B1}(\epsilon_n) \\ \Omega_{mn}^9(\mathbf{k}) &= C_{B2}^*(\epsilon_m)C_{B3}(\epsilon_n) + C_{B3}^*(\epsilon_m)C_{B2}(\epsilon_n),\end{aligned}$$

where the $C_i(\epsilon_m)$ are the Bloch wave coefficients of the m -band:

$$|\Psi_m(\mathbf{k})\rangle = \frac{1}{\sqrt{N_c}} \sum_{\alpha,i} C_{\alpha i}(\epsilon_m) \sum_n e^{i\mathbf{k}\cdot(\mathbf{R}_n + \mathbf{d}_{\alpha i})} |\phi_{n\alpha i}\rangle, \quad (\text{A1})$$

where $|\phi_{n\alpha i}\rangle = |\phi(\mathbf{r} - \mathbf{R}_n - \mathbf{d}_{\alpha i})\rangle$. The symmetries of the pairing amplitudes are determined by these coefficients which carry the information of the lattice symmetries. From the eigenvalues of Γ , $\frac{1}{J_\lambda}$, we obtain the Cooper pair formation energy, \tilde{J}_λ , in each channel pairing λ . The smaller the \tilde{J}_λ , the easier it is to form Cooper pairs in the corresponding channel. Hence, we can determine the dominant pairing channels allowed by symmetry given in Table I.

We illustrate in detail the $J' = J$ case which is amenable to analytical analysis. The structure of the Γ matrix in Eq. (28) is:

$$\Gamma = \begin{pmatrix} A_{3\times 3} & B_{3\times 3} & C_{3\times 3} \\ B_{3\times 3}^\dagger & D_{3\times 3} & -B_{3\times 3}^\dagger \\ C_{3\times 3} & -B_{3\times 3} & A_{3\times 3} \end{pmatrix}$$

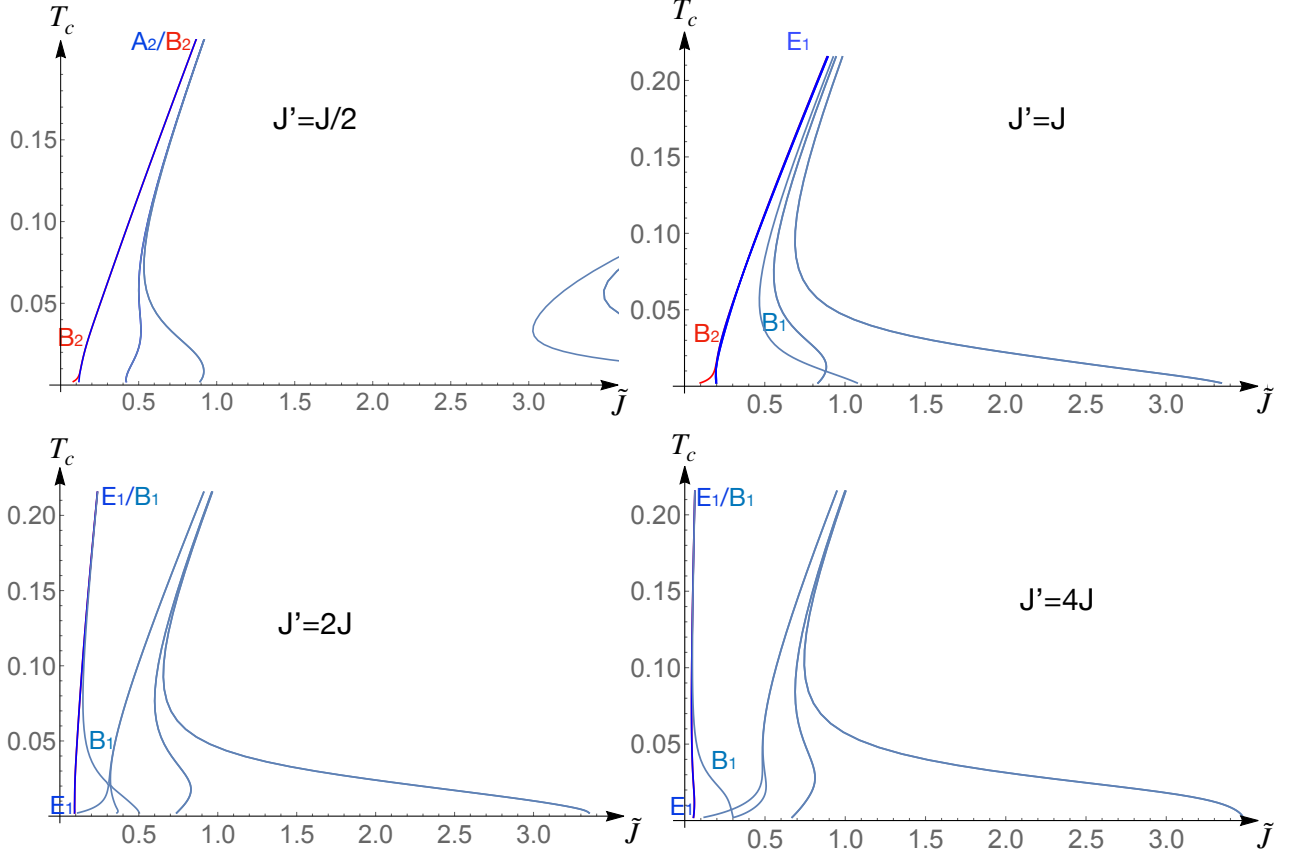


FIG. 12. Dependence of the critical temperatures in different pairing channels on the strength of the magnetic coupling, \tilde{J} , for different ratios J'/J at $\delta = 0.04$ obtained from the linearized gap equations. The most favorable solution at a given \tilde{J} occurs for the channel with the highest T_c .

where:

$$A_{3 \times 3} = \begin{pmatrix} a_1 & a_2 & a_2 \\ a_2 & a_1 & a_2 \\ a_2 & a_2 & a_1 \end{pmatrix}, \quad (\text{A2})$$

$$B_{3 \times 3} = \begin{pmatrix} 0 & b_1 & -b_1 \\ -b_1 & 0 & b_1 \\ b_1 & -b_1 & 0 \end{pmatrix}, \quad (\text{A3})$$

$$C_{3 \times 3} = \begin{pmatrix} c_1 & c_2 & c_2 \\ c_2 & c_1 & c_2 \\ c_2 & c_2 & c_1 \end{pmatrix}, \quad (\text{A4})$$

and

$$D_{3 \times 3} = \begin{pmatrix} d_1 & d_2 & d_2 \\ d_2 & d_1 & d_2 \\ d_2 & d_2 & d_1 \end{pmatrix}. \quad (\text{A5})$$

From the common eigenvectors: ϕ_{sym} , of the A, B, C, D matrices and their corresponding eigenvalues: $\tilde{a}_{sym}, \tilde{b}_{sym}, \tilde{c}_{sym}$ and \tilde{d}_{sym} we can find solutions analytically. Introducing: $[\Delta_\lambda]^\top = (\phi_{sym}, (0, 0, 0), \pm\phi_{sym})$ in Eq. (27) leads to the A_2

and B_2 solutions:

$$\begin{aligned} [\Delta(A_2)]^\top &\propto [(1, 1, 1), (0, 0, 0), (1, 1, 1)] \\ [\Delta(B_2)]^\top &\propto [(1, 1, 1), (0, 0, 0), (-1, -1, -1)] \end{aligned} \quad (\text{A6})$$

with corresponding eigenvalues:

$$\begin{aligned} \frac{1}{\tilde{J}_{A_2}} &= \tilde{a}_{sym} + \tilde{c}_{sym} = a_1 + 2a_2 + (c_1 + 2c_2), \\ \frac{1}{\tilde{J}_{B_2}} &= \tilde{a}_{sym} - \tilde{c}_{sym} = a_1 + 2a_2 - (c_1 + 2c_2). \end{aligned} \quad (\text{A7})$$

There are also two degenerate solutions of the E_2 type:

$$\begin{aligned} [\Delta(E_2)]^\top &\propto [(-1, 0, 1), (0, 0, 0), (-1, 0, 1)] \\ [\Delta(E_2)]^\top &\propto [(1, -1, 0), (0, 0, 0), (1, -1, 0)] \end{aligned} \quad (\text{A8})$$

with the common eigenvalue:

$$\frac{1}{\tilde{J}_{E_2}} = a_1 - a_2 + c_1 - c_2. \quad (\text{A9})$$

Finally, we find the B_1 solution:

$$[\Delta(B_1)]^\top \propto [(0, 0, 0), (1, 1, 1), (0, 0, 0)], \quad (\text{A10})$$

with eigenvalue

$$\frac{1}{\tilde{J}_{B_1}} = d_1 + 2d_2. \quad (\text{A11})$$

So we have found five solutions of the type $[\Delta_\lambda]^\top = (\phi_{sym}, (0, 0, 0), \pm\phi_{sym})$. There are four more solutions of the E_1 type:

$$\begin{aligned} [\Delta(E_1^-)]^\top &\propto ((1, 0, -1), (\beta, -2\beta, \beta), (-1, 0, 1)) \\ [\Delta(E_1^-)]^\top &\propto ((1, -1, 0), (-\beta, -\beta, 2\beta), (-1, 1, 0)) \\ [\Delta(E_1^+)]^\top &\propto ((1, 0, -1), (-\alpha, 2\alpha, -\alpha), (-1, 0, 1)) \\ [\Delta(E_1^+)]^\top &\propto ((1, -1, 0), (\alpha, \alpha, -2\alpha), (1, -1, 0)) \end{aligned}$$

$$\begin{aligned} \frac{1}{\tilde{J}_{E_1^-}} &= \frac{1}{2} \left(a_1 - a_2 - c_1 + c_2 + d_1 - d_2 - \sqrt{(a_1 - a_2 - c_1 + c_2 + d_1 - d_2)^2 + 24b_1^2 - 4(a_1 - a_2 - c_1 + c_2)(d_1 - d_2)} \right) \\ \frac{1}{\tilde{J}_{E_1^+}} &= \frac{1}{2} \left(a_1 - a_2 - c_1 + c_2 + d_1 - d_2 + \sqrt{(a_1 - a_2 - c_1 + c_2 + d_1 - d_2)^2 + 24b_1^2 - 4(a_1 - a_2 - c_1 + c_2)(d_1 - d_2)} \right) \end{aligned}$$

In Fig. 12 we show the dependence of T_c on the coupling strength for different anisotropies, $J'/J = 0.5, 1, 2$, and 4. We first discuss the results at weak coupling, $\tilde{J} \rightarrow 0$, which would correspond to large δ regime of Fig. 4 due to the GA projection. The T_c of the B_2 solution (red solid line) is the highest for small \tilde{J} when $J', J = 0.5, 1$ or 1.5 (the weak coupling results for $J' = 1.5J$ and shown in Fig. 9). However, for $J' = 2J$, the E_1 solution becomes more stable than the B_2 as $\tilde{J} \rightarrow 0$. These results indicate that the B_2 solution is stable in a broad range of J'/J consistent with the full phase diagrams of Fig. 4.

On the other hand, as \tilde{J} increases, other solutions become favoured. For $J' = J/2$ the T_c s of the B_2 and the A_2 merge so that both solutions are favorable, for $J' = J$ the E_1 is singled out having the highest T_c among all solutions. We also note how the T_c of the B_1 becomes the next most highest. In fact, for $J'/J = 2, 4$, the T_c of the B_1 converges to the T_c of the E_1 within the ranges of the plot. This analysis is consistent with the E_1 and E_1+B_1 solutions found at small doping, δ in the phase diagrams of Fig. 4 and the competition between these solutions as J'/J is varied shown in the phase diagrams of Fig. 6.

Appendix B: Exact diagonalization analysis

Here we give some details on the exact diagonalization calculations of model (1) at half-filling on small clusters. The ground state wavefunction and energy is compared with the [nn-tRVB] [Eq. (6)]. On the six-site cluster we have 20 pos-

where $\alpha \neq \beta$ in general. The above four states have corresponding eigenvalues:

sible spin configurations:

$$\begin{aligned} |1\rangle &= c_{1\uparrow}^\dagger c_{2\uparrow}^\dagger c_{3\uparrow}^\dagger c_{4\downarrow}^\dagger c_{5\downarrow}^\dagger c_{6\downarrow}^\dagger |0\rangle \\ |2\rangle &= c_{1\uparrow}^\dagger c_{2\uparrow}^\dagger c_{3\downarrow}^\dagger c_{4\uparrow}^\dagger c_{5\downarrow}^\dagger c_{6\downarrow}^\dagger |0\rangle \\ |3\rangle &= c_{1\uparrow}^\dagger c_{2\uparrow}^\dagger c_{3\downarrow}^\dagger c_{4\downarrow}^\dagger c_{5\uparrow}^\dagger c_{6\uparrow}^\dagger |0\rangle \\ |4\rangle &= c_{1\uparrow}^\dagger c_{2\uparrow}^\dagger c_{3\downarrow}^\dagger c_{4\downarrow}^\dagger c_{5\downarrow}^\dagger c_{6\uparrow}^\dagger |0\rangle \\ |5\rangle &= c_{1\uparrow}^\dagger c_{2\downarrow}^\dagger c_{3\uparrow}^\dagger c_{4\uparrow}^\dagger c_{5\downarrow}^\dagger c_{6\downarrow}^\dagger |0\rangle \\ |6\rangle &= c_{1\uparrow}^\dagger c_{2\downarrow}^\dagger c_{3\uparrow}^\dagger c_{4\downarrow}^\dagger c_{5\downarrow}^\dagger c_{6\downarrow}^\dagger |0\rangle \\ |7\rangle &= c_{1\uparrow}^\dagger c_{2\downarrow}^\dagger c_{3\uparrow}^\dagger c_{4\downarrow}^\dagger c_{5\downarrow}^\dagger c_{6\uparrow}^\dagger |0\rangle \\ |8\rangle &= c_{1\uparrow}^\dagger c_{2\downarrow}^\dagger c_{3\downarrow}^\dagger c_{4\uparrow}^\dagger c_{5\uparrow}^\dagger c_{6\downarrow}^\dagger |0\rangle \\ |9\rangle &= c_{1\uparrow}^\dagger c_{2\downarrow}^\dagger c_{3\downarrow}^\dagger c_{4\uparrow}^\dagger c_{5\downarrow}^\dagger c_{6\uparrow}^\dagger |0\rangle \\ |10\rangle &= c_{1\uparrow}^\dagger c_{2\downarrow}^\dagger c_{3\downarrow}^\dagger c_{4\downarrow}^\dagger c_{5\uparrow}^\dagger c_{6\uparrow}^\dagger |0\rangle \\ |11\rangle &= c_{1\downarrow}^\dagger c_{2\uparrow}^\dagger c_{3\uparrow}^\dagger c_{4\uparrow}^\dagger c_{5\downarrow}^\dagger c_{6\downarrow}^\dagger |0\rangle \\ |12\rangle &= c_{1\downarrow}^\dagger c_{2\uparrow}^\dagger c_{3\uparrow}^\dagger c_{4\downarrow}^\dagger c_{5\uparrow}^\dagger c_{6\downarrow}^\dagger |0\rangle \\ |13\rangle &= c_{1\downarrow}^\dagger c_{2\uparrow}^\dagger c_{3\uparrow}^\dagger c_{4\downarrow}^\dagger c_{5\downarrow}^\dagger c_{6\uparrow}^\dagger |0\rangle \\ |14\rangle &= c_{1\downarrow}^\dagger c_{2\uparrow}^\dagger c_{3\downarrow}^\dagger c_{4\uparrow}^\dagger c_{5\uparrow}^\dagger c_{6\downarrow}^\dagger |0\rangle \\ |15\rangle &= c_{1\downarrow}^\dagger c_{2\uparrow}^\dagger c_{3\downarrow}^\dagger c_{4\uparrow}^\dagger c_{5\downarrow}^\dagger c_{6\uparrow}^\dagger |0\rangle \\ |16\rangle &= c_{1\downarrow}^\dagger c_{2\uparrow}^\dagger c_{3\downarrow}^\dagger c_{4\downarrow}^\dagger c_{5\uparrow}^\dagger c_{6\uparrow}^\dagger |0\rangle \\ |17\rangle &= c_{1\downarrow}^\dagger c_{2\downarrow}^\dagger c_{3\uparrow}^\dagger c_{4\uparrow}^\dagger c_{5\uparrow}^\dagger c_{6\downarrow}^\dagger |0\rangle \\ |18\rangle &= c_{1\downarrow}^\dagger c_{2\downarrow}^\dagger c_{3\uparrow}^\dagger c_{4\uparrow}^\dagger c_{5\downarrow}^\dagger c_{6\uparrow}^\dagger |0\rangle \\ |19\rangle &= c_{1\downarrow}^\dagger c_{2\downarrow}^\dagger c_{3\uparrow}^\dagger c_{4\downarrow}^\dagger c_{5\uparrow}^\dagger c_{6\uparrow}^\dagger |0\rangle \\ |20\rangle &= c_{1\downarrow}^\dagger c_{2\downarrow}^\dagger c_{3\downarrow}^\dagger c_{4\uparrow}^\dagger c_{5\uparrow}^\dagger c_{6\uparrow}^\dagger |0\rangle. \end{aligned} \quad (\text{B1})$$

where $|0\rangle$ is the vacuum state. The ground state of the easy-plane ferromagnetic model is indeed the expected triplet $S = 1, S_z = 0$ which is described as:

$$|\Psi_0\rangle = \sum_n a_n |n\rangle. \quad (\text{B2})$$

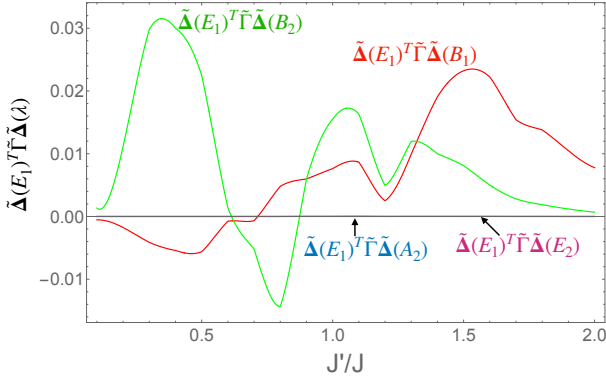


FIG. 13. Dependence on J'/J of the hybridization between the gap functions associated with the irreducible representations of C_{6v} on the DHL. The matrix elements of Eq. (C2) with $\lambda = E_1$ and $\lambda' = B_1, B_2, A_2$ and E_2 are plotted for $\delta = 0.04$ and $T/t = 0.01 < T_c$. Note that only the E_1 - B_1 and E_1 - B_2 matrix elements are non-zero indicating the possibility of hybrid $p + f$ (E_1+B_1 and E_1+B_2) superconducting states, and ruling out $p + i$ (E_1+A_2) or $p + d$ (E_1+E_2) superconductivity.

where the coefficients are: $A = A_{17} = A_{22} = A_{15} = A_{11} = A_{36} = A_4 = 0.3165$; $B = A_{19} = A_{18} = A_{16} = A_{14} = A_{13} = A_{12} = A_9 = A_8 = A_7 = A_5 = A_3 = A_2 = 0.17667$; and $C = A_1 = A_{20} = 0.1106$. The exact energy of the anisotropic FM model with $J' = J$ is $\epsilon_0(\text{exact}) = -3.541287J$. The exact wavefunction compares well with the normalized $|\text{n-trVB}\rangle$ state whose non-zero coefficients are $A = 0.3638$ and $B = C = 0.1212$ giving the overlap $|\langle \text{trVB} | \Psi_0 \rangle| = 0.9747$ quoted in Sec. III A.

Appendix C: Hybrid superconducting states

As well as the pure pairing states allowed by crystal symmetry, the SCE also yield solutions involving more than one irreducible representations of the C_{6v} group. As shown Fig. 4, two $p + f$ (E_1+B_1 and E_1+B_2) states occur for $J' = J$. Naively one would expect that only solutions belonging to the same irreducible representation of the character table I are allowed. However, this is only true for the linearized gap equations (26) at T_c since, in that case, the irreducible representations are eigenfunctions of the Γ -matrix. This is because Eq. (26) obeys the full C_{6v} symmetry of the DHL lattice (since it only depends on the bare band dispersions of the DHL).

However, for $T < T_c$, i.e., once superconductivity has set in, the C_{6v} symmetry of the system is spontaneously lowered to a new group, \mathcal{G} , which is a subgroup of C_{6v} . Thus, superconducting orders associated with different irreducible representations of C_{6v} may mix, if and only if the are in the same irreducible representation of \mathcal{G} . In order to explore possible mixing of superconducting orders we follow [55] and compute the matrix elements connecting different irreducible representations via a modified Γ matrix that explicitly contains the

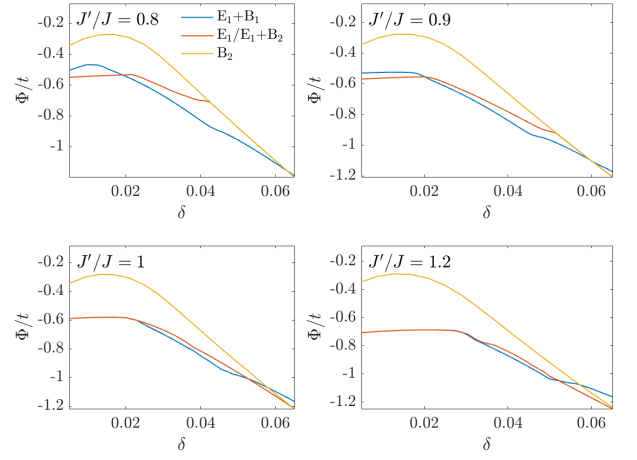


FIG. 14. Dependence of the free energies on δ of the most favorable pairing states found in the SCE analysis.

symmetry breaking due to the superconducting order,

$$\tilde{\Gamma}_{pq} = \frac{1}{2N_s} \frac{\tilde{J}_p}{\tilde{J}} \sum_{m,n,\mathbf{k}} \tanh\left(\frac{\omega_m(\mathbf{k})}{2k_B T}\right) \frac{1}{\epsilon_m(\mathbf{k}) + \epsilon_n(\mathbf{k})} \times (\Omega_{mn}^{*p}(\mathbf{k})\Omega_{mn}^q(\mathbf{k}) + \Omega_{mn}^p(\mathbf{k})\Omega_{mn}^{*q}(\mathbf{k})), \quad (\text{C1})$$

where $\omega_m(\mathbf{k})$ is given by the second order expression (25) with $\Delta_{mn}(\mathbf{k})$ evaluated with the real space gap function, $\Delta(\gamma)$. Note that this expression is appropriate to describe superconducting order below T_c since $\omega_m(\mathbf{k})$ enters this expression in the place of ϵ_m in the expression for Γ (Eq. (28)).

Taking $\Delta(\lambda)$ as the dominant gap function, i.e., the one with the highest T_c , we evaluate matrix elements with the rest of gap functions of the character table I. These matrix elements read:

$$\tilde{\Delta}(\lambda)^T \tilde{\Gamma} \tilde{\Delta}(\lambda'). \quad (\text{C2})$$

If the matrix element between $\tilde{\Delta}(\lambda)$ and $\tilde{\Delta}(\lambda')$ is non-zero then the two pairing solutions are allowed to hybridize below T_c .

As a relevant example to the phase diagrams of Fig. 4, we evaluate the matrix elements taking $\lambda = E_1$ since this is the most favorable pure state, i.e., the irreducible representation with the highest T_c for large \tilde{J} for $J'/J = 1$ or 1.5 (see Fig. 8 and 9). The dependence of matrix elements on J'/J for $T = 0.01t$ and a fixed hole doping of $\delta = 0.05$ is shown in Fig. 13. We first note that while matrix elements between E_1 and B_1 or B_2 states are non-zero, there is no hybridization with A_2 and E_2 states. This shows that hybrid $p + f$ (E_1+B_1 or E_1+B_2) states are allowed below T_c but $p + d$ (E_1+E_2) and $p + i$ (E_1+A_2) states are not. This is consistent with the phase diagrams, Fig. 4. Since the E_1/B_1 hybridization is comparable to the E_1/B_2 around $J' = J$ we can expect both combinations to occur. On the other hand, although around $J' = 1.5J$ the E_1/B_1 hybridization is strong, it is the E_1 solution that wins in the SCE analysis as Fig. 4 shows.

The analysis above is then useful to predict which pairing states may combine below T_c due to spontaneous symmetry breaking in the most favorable channel. This can be done before getting into the solution of the numerically cumbersome SCEs.

We now provide more details about the hybrid superconducting states obtained from the full SCEs. In Fig. 14 we

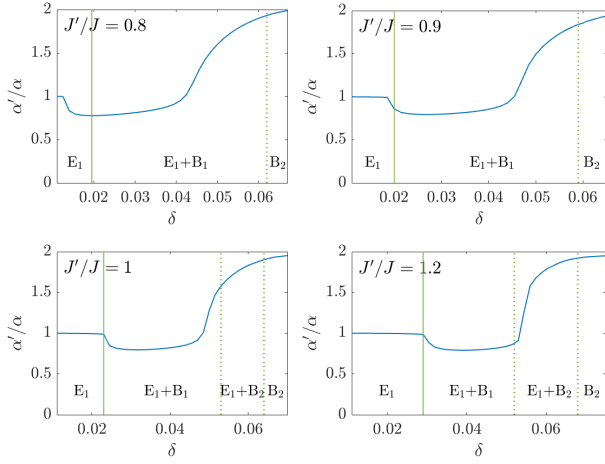


FIG. 15. Dependence of the parameters in the E_1+B_1 order parameter (Eq. (23)), α'/α , on δ for different J'/J . The first (dotted green line) and second (solid green line) order transitions separating the superconducting states are found from the free energy analysis of Fig. 14.

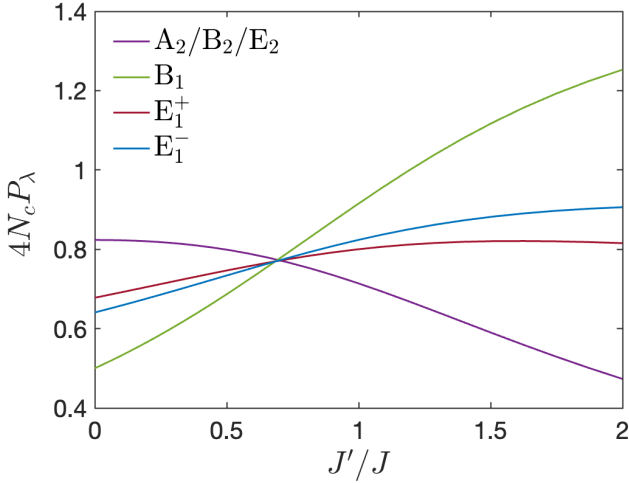


FIG. 16. Triplet pairing correlations dependence on J'/J of the half-filled Hubbard model (2) on a six-site cluster. Note that the degeneracy of the E_1^- and E_1^+ is lifted on the six-site cluster at this has C_{2v} symmetry rather than the C_{6v} symmetry of the full lattice. Nevertheless we retain the C_{6v} labels to retain straightforward connection to the rest of the manuscript.

$$P_\lambda = \frac{1}{4N_c} \sum_{\langle \alpha i, \beta j \rangle} \sum_{\langle \gamma k, \delta l \rangle} \Delta_{\alpha i, \beta j}(\lambda) \Delta_{\gamma k, \delta l}(\lambda) \left(\langle c_{\alpha i \uparrow}^\dagger c_{\beta j \downarrow}^\dagger c_{\gamma k \uparrow} c_{\delta l \downarrow} \rangle - \langle c_{\alpha i \uparrow}^\dagger c_{\gamma k \uparrow} \rangle \langle c_{\beta j \downarrow}^\dagger c_{\delta l \downarrow} \rangle \right) \quad (D1)$$

where $N_c = 6$, $\alpha, \beta, \gamma, \delta = A, B$, $i, j, k, l = 1, 2, 3$ and $\lambda = 1, \dots, 9$. The nine-component vector Δ_λ contains the pairing solutions obtained from the linearized equations of Sec. IV D which are described in Appendix A. The correspondence between the vector components of Δ and the Cooper paired bonds $(\alpha i, \beta j)$ are indicated in Eq. (12). As well as the

compare the free energies of the most favorable states around $J'/J = 1$ where the hybrid superconducting states are stabilised consistent with the weak coupling analysis just provided above. For $J'/J = 0.8$ and $J'/J = 0.9$ the E_1+B_1 state has the lowest energy in the doping range $0.02 < \delta < 0.06$ sandwiched between an E_1 and a B_2 . On the other hand, for $J'/J = 1$ and $J'/J = 1.2$, the E_1+B_2 hybrid state is most favorable between the E_1+B_1 and the B_2 . A first order transition from the E_1+B_1 to the E_1 solution occurs at $\delta \sim 0.02$ for $J'/J = 0.8, 0.9$, which becomes second order for $J'/J = 1, 1.2$ consistent with the behavior shown in the phase diagrams of Fig. 4.

Finally we consider in detail the properties of the E_1+B_1 state which is the most robust hybrid superconducting state found in the SCE. The dependence of α'/α ratios describing the mixed E_1+B_1 gap function (Eq. (23)) is plotted in Fig. 15 for the same J'/J as shown in Fig. 14. The smooth variation of α'/α with δ indicates that the hybrid E_1+B_1 state is not an artifact of the numerical solution of the SCE. Superconducting transitions occur concomitantly with the phase transitions identified from the free energies plotted in Fig 14 as expected.

Appendix D: Pairing correlations from exact diagonalization on small clusters

Following our previous work [36] we explore unconventional triplet pairing using ED techniques on the half-filled Hubbard model with imaginary hopping amplitudes (2). As explained in Sec. II this model, at half-filling, maps onto the easy-plane ferromagnetic XXZ model (3). We have checked through ED calculations that indeed the two models share the same ground state for $U \gg t, t'$.

In order to elucidate the pairing symmetry of the tRVB state as $\delta \rightarrow 0$ we compute the pairing correlations which can be obtained exactly by evaluating[59]:

expected value of the product of the creation and annihilation pairing operators, note that there is a subtracted term which suppresses the contribution from the $i = j$ pairing amplitudes. Although these are substantial in small clusters, they are less important for quantifying actual superconducting correlations in the extended lattice.

Fig. 16 illustrates the dependence of the triplet pairing correlations of the half-filled Hubbard model (2) on a six-site cluster with $J'/J \propto \lambda'^2/\lambda^2$. The largest pairing correlations in a given channel, λ , P_λ , indicates that it is the most favorable at a given J'/J . The pairing correlations associated with the spatial symmetries A_2 , B_2 and E_2 are degenerate in the whole J'/J range explored due to the absence of inter-triangle pairing amplitudes in these solutions making them indistinguishable on a six-site cluster. The results of Fig. 16 show that while the A_2 , B_2 and E_2 solutions are favored for $J'/J \leq 1/\sqrt{2}$, the B_1 followed by an E_1 dominates for $J'/J > 1/\sqrt{2}$. This change of solutions with J'/J is in overall qualitative agreement with the predictions of the linearized gap equations, Fig. 12.

Appendix E: Chern number in superconducting states

In a discretized Brillouin zone, the total Chern number ν can be calculated from the Berry phases γ_{nl} at each elementary placquette l . The Berry phase is the accumulated phase of the wave function along a closed k -path.

$$\gamma_{nl} = \text{Im} \ln \prod_{j=0}^{N-1} \langle u_{\mathbf{nk}_j} | u_{\mathbf{nk}_{j+1}} \rangle \quad (\text{E1})$$

where n is the band index and the loop chosen is rectangular with $N = 4$. In the multiband case the wave functions overlap of all possible combinations must be taken into account. Thus we construct a $N_c \times N_c$ matrix at each step of the path, where N_c is the number of occupied bands. Then, the Berry phase is just the phase of the determinant of the product of these matrices along the loop. The Chern number is the sum over the first Brillouin zone (FBZ) of all those Berry phases:

$$\nu = \frac{1}{2\pi} \sum_{\text{FBZ}} \text{Im} \ln \det \prod_{j=0}^3 \langle u_{\mathbf{mk}_j} | u_{\mathbf{nk}_{j+1}} \rangle \quad (\text{E2})$$

where $1 \leq m, n \leq N_c$.

The Chern number ν of a 2-dimensional superconductor with broken time-reversal symmetry can be computed following the exact procedure stated above but replacing $|u_{\mathbf{nk}}\rangle$ by the Bogoliubov quasiparticle wave functions.[60]

-
- [1] M. R. Norman, D. Pines, and C. Kallin, The pseudogap: friend or foe of high T_c ?, *Adv. Phys.* **54**, 715 (2005).
- [2] P. A. Lee, N. Nagaosa, and X.-G. Wen, Doping a mott insulator: Physics of high-temperature superconductivity, *Rev. Mod. Phys.* **78**, 17 (2006).
- [3] M. Ogata and H. Fukuyama, The t-J model for the oxide high- T_c superconductors, *Rep. Prog. Phys.* **71**, 036501 (2008).
- [4] B. J. Powell and R. H. McKenzie, Quantum frustration in organic mott insulators: from spin liquids to unconventional superconductors, *Rep. Prog. Phys.* **74**, 056501 (2011).
- [5] Y. Cao, V. Fatemi, A. Demir, S. Fang, S. L. Tomarken, J. Y. Luo, J. D. Sanchez-Yamagishi, K. Watanabe, T. Taniguchi, E. Kaxiras, R. C. Ashoori, and P. Jarillo-Herrero, Correlated insulator behaviour at half-filling in magic-angle graphene superlattices, *Nature* **556**, 80 (2018).
- [6] Y. Cao, V. Fatemi, S. Fang, K. Watanabe, T. Taniguchi, E. Kaxiras, and P. Jarillo-Herrero, Unconventional superconductivity in magic-angle graphene superlattices, *Nature* **556**, 43 (2018).
- [7] R. H. McKenzie, Similarities between organic and cuprate superconductors, *Science* **278**, 820 (1997).
- [8] Y. Kurosaki, Y. Shimizu, K. Miyagawa, K. Kanoda, and G. Saito, Mott transition from a spin liquid to a fermi liquid in the spin-frustrated organic conductor κ -(ET)₂Cu₂(CN)₃, *Phys. Rev. Lett.* **95**, 177001 (2005).
- [9] Y. Shimizu, T. Hiramatsu, M. Maesato, A. Otsuka, H. Yamochi, A. Ono, M. Itoh, M. Yoshida, M. Takigawa, Y. Yoshida, and G. Saito, Pressure-tuned exchange coupling of a quantum spin liquid in the molecular triangular lattice κ -(ET)₂Ag₂(CN)₃, *Phys. Rev. Lett.* **117**, 107203 (2016).
- [10] P. W. Anderson, The resonating valence bond state in La₂CuO₄ and superconductivity, *Science* **235**, 1196 (1987).
- [11] B. J. Powell and R. H. McKenzie, Symmetry of the superconducting order parameter in frustrated systems determined by the spatial anisotropy of spin correlations, *Phys. Rev. Lett.* **98**, 027005 (2007).
- [12] P. Anderson, Resonating valence bonds: A new kind of insulator?, *Mater. Res. Bull.* **8**, 153 (1973).
- [13] L. Balents, C. Dean, D. Efetov, and Y. A. F., Superconductivity and strong correlations in moiré flat bands, *Nat. Phys.* **16**, 725–733 (2020).
- [14] A. J. Leggett, Nobel lecture: Superfluid ³He: the early days as seen by a theorist, *Rev. Mod. Phys.* **76**, 999 (2004).
- [15] A. J. Leggett, A theoretical description of the new phases of liquid ³He, *Rev. Mod. Phys.* **47**, 331 (1975).
- [16] A. P. Mackenzie, T. Scaffidi, C. W. Hicks, and Y. Maeno, Even odder after twenty-three years: the superconducting order parameter puzzle of Sr₂RuO₄, *npj Quantum Mater.* **2**, 40 (2017).
- [17] A. P. Mackenzie and Y. Maeno, The superconductivity of Sr₂RuO₄ and the physics of spin-triplet pairing, *Rev. Mod. Phys.* **75**, 657 (2003).
- [18] A. Pustogow, Y. Luo, A. Chronister, Y.-S. Su, D. A. Sokolov, F. Jerzembeck, A. P. Mackenzie, C. W. Hicks, N. Kikugawa, S. Raghu, E. D. Bauer, and S. E. Brown, Constraints on the superconducting order parameter in Sr₂RuO₄ from oxygen-17 nuclear magnetic resonance, *Nature* **574**, 72 (2019).
- [19] J. Wosnitzer, Superconductivity of organic charge-transfer salts, *J. Low Temp. Phys.* **197**, 250 (2019).

- [20] J.-K. Bao, J.-Y. Liu, C.-W. Ma, Z.-H. Meng, Z.-T. Tang, Y.-L. Sun, H.-F. Zhai, H. Jiang, H. Bai, C.-M. Feng, Z.-A. Xu, and G.-H. Cao, Superconductivity in quasi-one-dimensional $K_2Cr_3As_3$ with significant electron correlations, *Phys. Rev. X* **5**, 011013 (2015).
- [21] J. Yang, J. Luo, C. Yi, Y. Shi, Y. Zhou, and G. qing Zheng, Spin-triplet superconductivity in $K_2Cr_3As_3$, *Sci. Adv.* **7**, eabl4432 (2021).
- [22] W. Cai, H. Sun, W. Xia, C. Wu, Y. Liu, H. Liu, Y. Gong, D.-X. Yao, Y. Guo, and M. Wang, Pressure-induced superconductivity and structural transition in ferromagnetic $CrSiTe_3$, *Phys. Rev. B* **102**, 144525 (2020).
- [23] E. J. König, Y. Komijani, and P. Coleman, Triplet resonating valence bond theory and transition metal chalcogenides, *Phys. Rev. B* **105**, 075142 (2022).
- [24] S. H. Lin Jiao, S. Ran, Z. Wang, J. O. Rodriguez, M. Sigrist, Z. Wang, N. P. Butch, and V. Madhavan, Chiral superconductivity in heavy-fermion metal UTe_2 , *Nature* **579**, 523–527 (2020).
- [25] D. Aoki, K. Ishida, and J. Flouquet, Review of u-based ferromagnetic superconductors: Comparison between UGe_2 , $urhge$, and $ucoge$, *Journal of the Physical Society of Japan* **88**, 022001 (2019), <https://doi.org/10.7566/JPSJ.88.022001>.
- [26] P. Coleman, Y. Komijani, and E. J. König, Triplet resonating valence bond state and superconductivity in hund's metals, *Phys. Rev. Lett.* **125**, 077001 (2020).
- [27] P. W. Anderson, Further consequences of symmetry in heavy-electron superconductors, *Phys. Rev. B* **32**, 499 (1985).
- [28] S. A. Baudron, P. Batail, C. Coulon, R. Clérac, E. Canadell, V. Laukhin, R. Melzi, P. Wzietek, D. Jérôme, P. Auban-Senzier, and S. Ravy, (edt-ttf-conh2)6[re6se8(cn)6], a metallic kagome-type organic-inorganic hybrid compound: Electronic instability, molecular motion, and charge localization, *Journal of the American Chemical Society* **127**, 11785 (2005), pMID: 16104757, <https://doi.org/10.1021/ja0523385>.
- [29] R. Llusar, S. Uriel, C. Vicent, J. M. Clemente-Juan, E. Coronado, C. J. Gómez-García, B. Braïda, and E. Canadell, Single-component magnetic conductors based on Mo_3S_7 trinuclear clusters with outer dithiolate ligands, *J. Am. Chem. Soc.* **126**, 12076 (2004).
- [30] Y. Shuku, A. Mizuno, R. Ushiroguchi, C. S. Hyun, Y. J. Ryu, B.-K. An, J. E. Kwon, S. Y. Park, M. Tsuchiizu, and K. Awaga, An exotic band structure of a supramolecular honeycomb lattice formed by a pancake π - π interaction between triradical trianions of triptycene tetrabenzoquinone, *Chem. Commun.* **54**, 3815 (2018).
- [31] M. F. López and J. Merino, Magnetism and topological phases in an interacting decorated honeycomb lattice with spin-orbit coupling, *Phys. Rev. B* **102**, 035157 (2020).
- [32] H. L. Nourse, R. H. McKenzie, and B. J. Powell, Multiple insulating states due to the interplay of strong correlations and lattice geometry in a single-orbital hubbard model, *Phys. Rev. B* **103**, L081114 (2021).
- [33] H. L. Nourse, R. H. McKenzie, and B. J. Powell, Spin-0 mott insulator to metal to spin-1 mott insulator transition in the single-orbital hubbard model on the decorated honeycomb lattice, *Phys. Rev. B* **104**, 075104 (2021).
- [34] M. Fernández López and J. Merino, Bad topological semimetals in layered honeycomb compounds, *Phys. Rev. B* **105**, 115138 (2022).
- [35] H. L. Nourse, R. H. McKenzie, and B. J. Powell, C_3 symmetry breaking metal-insulator transitions in a flat band in the half-filled hubbard model on the decorated honeycomb lattice, *Phys. Rev. B* **105**, 205119 (2022).
- [36] J. Merino, M. F. López, and B. J. Powell, Unconventional superconductivity near a flat band in organic and organometallic materials, *Phys. Rev. B* **103**, 094517 (2021).
- [37] A. L. Khosla, A. C. Jacko, J. Merino, and B. J. Powell, Spin-orbit coupling and strong electronic correlations in cyclic molecules, *Phys. Rev. B* **95**, 115109 (2017).
- [38] A. C. Jacko, A. L. Khosla, J. Merino, and B. J. Powell, Spin-orbit coupling in $Mo_3S_7(dmit)_3$, *Phys. Rev. B* **95**, 155120 (2017).
- [39] J. Merino, A. C. Jacko, A. L. Khosla, and B. J. Powell, Effects of anisotropy in spin molecular-orbital coupling on effective spin models of trinuclear organometallic complexes, *Phys. Rev. B* **96**, 205118 (2017).
- [40] B. J. Powell, J. Merino, A. L. Khosla, and A. C. Jacko, Heisenberg and dzyaloshinskii-moriya interactions controlled by molecular packing in trinuclear organometallic clusters, *Phys. Rev. B* **95**, 094432 (2017).
- [41] S. Rachel and K. Le Hur, Topological insulators and mott physics from the hubbard interaction, *Phys. Rev. B* **82**, 075106 (2010).
- [42] S. Trebst and C. Hickey, Kitaev materials, *Physics Reports* **950**, 1 (2022).
- [43] S. M. Winter, A. A. Tsirlin, M. Daghofer, J. van den Brink, Y. Singh, P. Gegenwart, and R. Valentí, Models and materials for generalized kitaev magnetism, *Journal of Physics: Condensed Matter* **29**, 493002 (2017).
- [44] T. Hazra and P. Coleman, Triplet pairing mechanisms from Hund's-Kondo models: applications to UTe_2 and $CeRh_2As_2$ [10.48550/arxiv.2205.13529](https://arxiv.org/abs/2205.13529) (2022).
- [45] A. C. Jacko, C. Janani, K. Koepernik, and B. J. Powell, Emergence of quasi-one-dimensional physics in a nearly-isotropic three-dimensional molecular crystal: Ab initio modeling of $Mo_3S_7(dmit)_3$, *Phys. Rev. B* **91**, 125140 (2015).
- [46] R. Shindou and T. Momoi, $SU(2)$ slave-boson formulation of spin nematic states in $S = 1/2$ frustrated ferromagnets, *Phys. Rev. B* **80**, 064410 (2009).
- [47] R. Moessner and K. S. Raman, Quantum dimer models. In C Lacroix, P Mendels, F Mila (Eds.). Introduction to frustrated magnetism: Materials, experiments, theory (Springer, Berlin, Heidelberg, 2011) Chap. 17, pp. 437–479.
- [48] B. J. Powell, Emergent particles and gauge fields in quantum matter, *Contemporary Physics* **61**, 96 (2020), <https://doi.org/10.1080/00107514.2020.1832350>.
- [49] S. S. Jahromi and R. Orús, Spin- $\frac{1}{2}$ heisenberg antiferromagnet on the star lattice: Competing valence-bond-solid phases studied by means of tensor networks, *Phys. Rev. B* **98**, 155108 (2018).
- [50] S.-O. Kaba and D. Sénéchal, Group-theoretical classification of superconducting states of strontium ruthenate, *Phys. Rev. B* **100**, 214507 (2019).
- [51] The f -wave superconducting state found in our previous paper [36] was incorrectly labeled as a B_2 but is in fact a B_1 (both are f -wave states). The nodal structure corresponds to an $f_{x(3y^2-3x^2)}$ cubic basis function.
- [52] G. Kotliar and J. Liu, Superexchange mechanism and d-wave superconductivity, *Phys. Rev. B* **38**, 5142 (1988).
- [53] B. J. Powell, A phenomenological model of the supercon-

- ducting state of the bechgaard salts, *Journal of Physics: Condensed Matter* **20**, 345234 (2008).
- [54] D. Vollhardt and P. Wolfe, *The superfluid phases of helium 3* (CRC Press, 1990).
- [55] M. Sigrist and K. Ueda, Phenomenological theory of unconventional superconductivity, *Rev. Mod. Phys.* **63**, 239 (1991), pages 250-251.
- [56] Y.-Z. You, I. Kimchi, and A. Vishwanath, Doping a spin-orbit mott insulator: Topological superconductivity from the kitaev-heisenberg model and possible application to $(\text{Na}_2/\text{Li}_2)\text{IrO}_3$, *Phys. Rev. B* **86**, 085145 (2012).
- [57] B. J. Powell, Mixed order parameters, accidental nodes and broken time reversal symmetry in organic superconductors: a group theoretical analysis, *Journal of Physics: Condensed Matter* **18**, L575 (2006).
- [58] H. Oike, Y. Suzuki, H. Taniguchi, Y. Seki, K. Miyagawa, and K. Kanoda, Anomalous metallic behaviour in the doped spin liquid candidate $\kappa\text{-(ET)}_4\text{Hg}_{2.89}\text{Br}_8$, *Nat. Commun.* **8**, 756 (2017).
- [59] J. Merino and O. Gunnarsson, Pseudogap and singlet formation in organic and cuprate superconductors, *Phys. Rev. B* **89**, 245130 (2014).
- [60] K. Lee, T. Hazra, M. Randeria, and N. Trivedi, Topological superconductivity in dirac honeycomb systems, *Phys. Rev. B* **99**, 184514 (2019).